TO APPEAR IN *The Astrophysical Journal*.
Preprint typeset using LaTeX style emulateapj v. 26/01/00

THE MASS FUNCTION OF ACTIVE BLACK HOLES IN THE LOCAL UNIVERSE

JENNY E. GREENE[1]
Department of Astrophysical Sciences, Princeton University, Princeton, NJ
LUIS C. HO
The Observatories of the Carnegie Institution of Washington, 813 Santa Barbara St., Pasadena, CA 91101

To appear in The Astrophysical Journal.

ABSTRACT

We present the first measurement of the black hole (BH) mass function for broad-line active galaxies in the local Universe. Using the ~ 9000 broad-line active galaxies from the Fourth Data Release of the Sloan Digital Sky Survey, we construct a broad-line luminosity function that agrees very well with the local soft X-ray luminosity function. Using standard virial relations, we then convert observed broad-line luminosities and widths into BH masses. A mass function constructed in this way has the unique capability to probe the mass region $< 10^6\ M_\odot$, which, while insignificant in terms of total BH mass density, nevertheless may place important constraints on the mass distribution of seed BHs in the early Universe. The characteristic local active BH has a mass of $\sim 10^7\ M_\odot$ radiating at 10% of the Eddington rate. The active fraction is a strong function of BH mass; at both higher and lower masses the active mass function falls more steeply than one would infer from the distribution of bulge luminosity. The deficit of local massive radiating BHs is a well-known phenomenon, while we present the first robust measurement of a decline in the space density of active BHs at low mass.

Subject headings: galaxies: active — galaxies: nuclei — galaxies: Seyfert

1. THE LOCAL BLACK HOLE MASS FUNCTION

There is strong evolution in both the number density and typical luminosity of active galactic nuclei (AGNs) over cosmic time (e.g., Ueda et al. 2003; Richards et al. 2006), but from luminosity functions alone it is difficult to determine whether mass or luminosity evolution is the predominant agent of these changes. One thing we do know is that the growth of black holes (BHs) and galaxies are coordinated such that, in local spheroids, BH mass is strongly correlated with spheroid luminosity (Marconi & Hunt 2003) and stellar velocity dispersion (the $M_{\rm BH}-\sigma_*$ relation; Gebhardt et al. 2000a; Ferrarese & Merritt 2000; Tremaine et al. 2002; Barth et al. 2005). Charting the mass accretion history of the Universe thus may provide important insight into the growth of galaxies. It has become possible, using the $M_{\rm BH}-\sigma_*$ relation, to calibrate virial scaling relations between AGN luminosity and the size of the broad-line region (Gebhardt et al. 2000b; Ferrarese et al. 2001; Onken et al. 2004; Nelson et al. 2004; Greene & Ho 2006b); these techniques have been used to investigate BH mass functions at intermediate to high redshift (e.g., Vestergaard 2004; McLure & Dunlop 2004; Kollmeier et al. 2006), but not in a systematic way for nearby systems. A good measurement of the local active BH mass function provides an essential boundary condition for models of the evolution in active BH mass. Furthermore, we can probe significantly further down the mass function at the present day than at any other epoch.

In fact, BH mass functions built from local broad-line AGN samples have the unique capability to probe BH masses $M_{\rm BH}\lesssim 10^{6.5}\ M_\odot$. Mass functions derived from stellar velocity dispersions (whether they be inactive [Yu & Tremaine 2002] or narrow-line active galaxies [Heckman et al. 2004]) are necessarily limited to the current spectral resolution limits of large-area spectroscopic surveys such as the Sloan Digital Sky Survey (SDSS; e.g., Bernardi et al. 2003). At the same time, the conversion from galaxy luminosity to BH mass is completely unconstrained at these low masses. Direct dynamical mass measurements in this mass range are beyond the spatial resolving power of current instrumentation for all but the nearest systems. Thus broad-line AGNs currently provide the only means to systematically explore the BH mass function below $10^6\ M_\odot$ ("intermediate-mass" BHs; e.g., Greene & Ho 2004). Although such objects constitute a negligible fraction of the present-day BH mass density, it is actually quite important to characterize the low-mass end of the local BH mass function. For one thing, it provides one of the only available observational constraints on models of the initial mass spectrum and halo occupation fraction of BH seeds in the early Universe (e.g., Volonteri et al. 2003). Furthermore, anisotropic gravitational radiation from unequal mass BH-BH mergers imparts a net linear angular momentum or "kick" to the merger remnant with a velocity that may exceed the escape velocity of dwarf galaxies (e.g., Favata et al. 2004; Merritt et al. 2004). We may test this picture with observational constraints on the number of local dwarf galaxies that host BHs.

Once we have characterized the zero-redshift broad-line BH mass function, we may investigate whether broad-line AGNs trace the same local population as samples selected by alternate means. For instance, we expect the soft X-ray luminosity to come from unobscured sources with broad lines, and thus we expect very similar luminosity functions for the two populations. Also, it would be instructive to compare our results to those of the complementary study of Heckman et al. (2004), which uses the $M_{\rm BH}-\sigma_*$ relation to infer the BH mass function for local narrow-line AGNs. Our methodology, based on AGN physics rather than indirectly on the $M_{\rm BH}-\sigma_*$ relation, provides an important alternate measure of the local active BH mass density. Furthermore, we may compare the space density of narrow- and broad-line objects as a function of mass; a well-

[1]Hubble and Princeton-Carnegie Fellow

matched comparison has never been performed in the literature before, and has interesting consequences for our understanding of AGN unification. Finally, as we shall see, the shape of the active and inactive (as inferred from galaxy luminosity functions) mass functions diverge, both at high and low mass. The mass-dependent active fraction contains useful information about the primary triggering mechanisms of active galaxies. By studying in detail the BHs that are radiating in the present-day Universe, we may hope to gain new insight into the strong evolution of BH growth with cosmic time.

We briefly review the methodology behind BH mass estimates in §2, then present our sample selection and methodology in §3, derive the luminosity and mass functions in §4, and discuss the implications in §5. We summarize and conclude in §6. Throughout we assume the following cosmological parameters to calculate distances: $H_0 = 100\,h = 71$ km s^{-1} Mpc^{-1}, $\Omega_{\rm m} = 0.27$, and $\Omega_\Lambda = 0.75$ (Spergel et al. 2003).

2. BLACK HOLE MASSES FOR ACTIVE GALAXIES

Compared to the dynamical masses used to calibrate the $M_{\rm BH}-\sigma_*$ relation, BH mass estimates using AGNs are rather crude, and some discussion of their validity is in order. So-called virial masses, $M_{\rm BH}=fR\upsilon^2/G$, are estimated using a relation between AGN luminosity and broad-line region radius (R; the radius-luminosity relation; e.g., Kaspi et al. 2005), combined with a measurement of the broad-line region (BLR) velocity dispersion (υ). The factor f accounts for the unknown broad-line region geometry and here is assumed to be 0.75, corresponding to a spherical broad-line region (Netzer 1990).

Although relying on the physics of the BLR to estimate BH masses is fraught with danger (e.g., Krolik 2001), it is possible to directly compare virial masses with the measurements of bulge stellar velocity dispersions, and calibrate them with the $M_{\rm BH}-\sigma_*$ relation. Rather remarkably, those reverberation-mapped AGNs with σ_* measurements show good agreement between the two mass indicators (Gebhardt et al. 2000b; Ferrarese et al. 2001; Onken et al. 2004; Nelson et al. 2004). Still, the total sample, across all above comparisons, consist of no more than 15 objects. For this reason Greene & Ho (2006b) directly compared σ_* with virial masses for 88 AGNs. They find the virial masses provide a good estimate of BH with a scatter of 0.4 dex, but a number of potential systematic effects remain.

The slope of the radius-luminosity relation is currently uncertain, primarily because it has been measured for only ~ 30 objects spanning a limited luminosity range. Most recently, Bentz et al. (2006) find a shallower radius-luminosity slope (0.52 ± 0.04 rather than the 0.64 ± 0.02 assumed here), which would lead to a narrower distribution in BH mass. For the typical Eddington ratio of our sources, $L_{\rm bol}/L_{\rm Edd}$=0.1, the Bentz et al. formalism shifts the BH masses upwards by ~ 0.3 dex for a $10^5\ M_\odot$ BH and downwards by ~ 0.2 dex for a $10^9\ M_\odot$ BH. However, as noted by Netzer & Trakhtenbrot (2007), if all objects included in the Kaspi et al. sample are included in the Bentz et al. analysis, the final slope is consistent with the Kaspi et al. result. Larger reverberation-mapped samples are urgently needed, but in the meantime we continue to use the steeper slope. The other outstanding uncertainty is related to the (unknown) geometry of the BLR, which translates into a different pre-factor f. Both Onken et al. (2004) and Greene & Ho (2006b) find that virial masses calculated assuming a spherical BLR (as we have done here) are too low by a factor of ~ 1.6, corresponding to a net increase in all BH masses of 0.2 dex. However, Collin et al. (2006) present some evidence that the BLR geometry is luminosity or Eddington-ratio dependent. As yet, there are not sufficient statistics to define a luminosity-dependent f factor, and so we prefer to apply no correction at this time.

3. SAMPLE SELECTION

The sample selection follows the technique of Greene & Ho (2004), which we summarize briefly here. Our parent sample is drawn from the Fourth Data Release (DR4) of the SDSS (York et al. 2002; Adelman-McCarthy et al. 2006), which includes spectroscopy of 565,715 objects classified as galaxies and 67,382 objects classified as AGNs with redshifts $z < 2.1$. We analyze all spectra with $z < 0.352$, although we remove those galaxies for which $> 20\%$ of the pixels between 6400–6700 Å have been flagged as bad by the SDSS pipeline; this results in a total of 544,127 spectra (including multiple observations of the same object). Following Greene & Ho (2004; see also Ho et al. 1997a), we begin by modeling and removing the stellar continuum, which may mask or mimic the presence of broad emission lines that we use as the signature of an accreting BH. We use the principal component analysis (PCA) method of Hao et al. (2005a) that encapsulates the variance in SDSS absorption-line galaxies in a set of eight orthogonal eigenspectra. The galaxy continua are modeled as linear combinations of these eigenspectra, a power-law to represent the AGN continuum, and a possible A-star component. We have not attempted to model the broad Fe II emission that is present throughout most of the optical spectrum (e.g., Boroson & Green 1992; Greene & Ho 2006a); while this is important for measurements of Hβ and [O III], the impact on the Hα region is negligible.

After galaxy subtraction, in order to limit the number of potential candidates, we employ an algorithm that identifies potential broad emission in the Hα region, based on an excess variance in the Hα region compared with the featureless continuum. The following analysis is performed over the spectral region 6400–6700 Å. Narrow emission-line flux is removed in an iterative scheme, in which points with fluxes $> 4\,\sigma$ (as measured in the entire spectral region) are replaced with the median value in the region, until there is $< 1\%$ decrease in σ, in practice taking no more than 5 iterations. This method of narrow emission line removal is conservative, in the sense that some flux from very strong narrow emission lines will remain. However, without a full spectral decomposition of the region, which we perform below, a single-Gaussian fit to the narrow emission lines may easily remove a relatively narrow broad component. We then smooth the spectrum with a 10-pixel boxcar to remove high-frequency noise and increase our sensitivity to real broad components. Those sources with a root-mean-square (rms) deviation that is 50% higher in the 6400–6700 Å region than in the regions 5500–6280Å (excluding 20 Å around the NaD λ5895 doublet) and 6900–7300 Å are kept, for a total of 31,750 spectra.

With this smaller subset of sources we perform more detailed modeling of the Hα+[N II] $\lambda\lambda$6548, 6583 region. Careful modeling of the narrow lines is crucial, since velocity structure in the narrow-line region can mimic broad lines (see additional arguments in Ho et al. 1997c and details of the methodology in Greene & Ho 2004, 2005a,b). Whenever possible, we build a multi-component Gaussian model for the narrow lines using the nearby [S II] $\lambda\lambda$6716, 6731 lines that empirically are found to provide a good model for the narrow Hα+[N II] (Filippenko

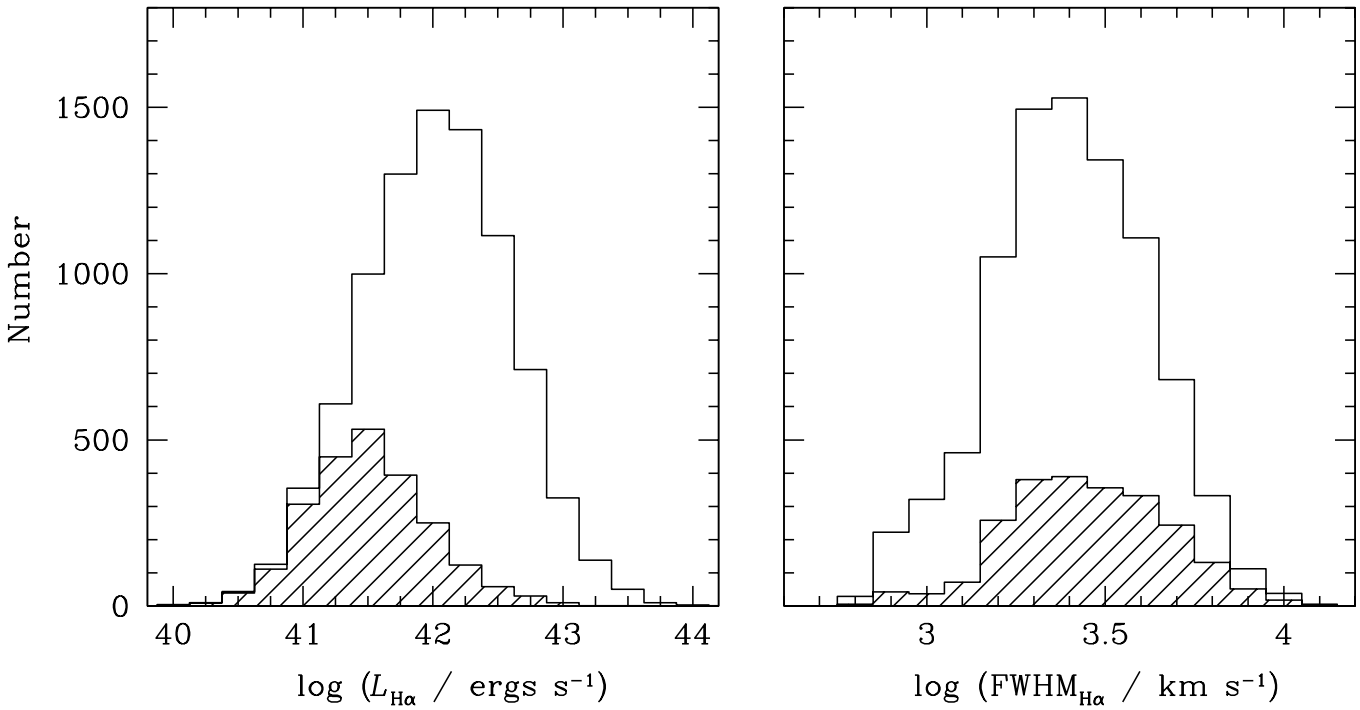

FIG. 1.— Distributions of broad $L_{H\alpha}$ (*left*) and broad FWHM$_{H\alpha}$ (*right*) for the entire sample of broad-line AGNs. The shaded histograms indicate the distribution of those objects targeted within the SDSS main galaxy sample. Note the dominance of objects with FWHM$_{H\alpha}$< 2000 km s^{-1}, the canonical division between classical and "narrow-line" Seyfert 1 galaxies.

& Sargent 1988; Ho et al. 1997c), and in cases without [S II] emission, we resort to using a model based on the core of the [O III] λ5007 line. The relative wavelengths of Hα and the [N II] doublet are fixed to laboratory values, as are the relative strength of the [N II] lines, and only the relative amplitudes of the Hα and [N II] lines are allowed to vary. We adopt the empirical criterion of Hao et al. (2005a) to determine whether an additional component is required: any component that results in a 20% decrease in χ^2 is deemed statistically justified. Broad lines are often lumpy and asymmetric, so we model the broad emission with multiple Gaussians, but attach no physical significance to any given component. All objects with broad Hα components apart from those in the narrow-line model are retained.

Table 1. The Sample

Name (1)	z (2)	FWHM$_{H\alpha}$ (3)	log $L_{H\alpha}$ (4)	log M_{BH} (5)
J000000.47−002703.9	0.250	2010	41.65	6.7
J000048.15−095404.0	0.206	2470	41.61	6.9
J000102.19−102326.8	0.294	5330	42.75	8.2

Note. — Col. (1): Name. Col. (2): Redshift. Col. (3): FWHM$_{H\alpha}$ (km s^{-1}). Col. (4): $L_{H\alpha}$ (ergs s^{-1}). Col. (5): $M_{BH} = (2.0\ ^{+0.4}_{-0.3}) \times 10^6\ M_\odot\ (L_{H\alpha}/10^{42}\ \mathrm{ergs\ s^{-1}})^{0.55\pm0.02}\ (\mathrm{FWHM}_{H\alpha}/10^3\ \mathrm{km\ s^{-1}})^{2.06\pm0.06}$ (Greene & Ho 2005b). Table 1 is available in its entirety via the link to the machine-readable table above. The following is included only as a guide to content and presentation.

Our goal is to limit our sample to those targets for whom we may estimate a reliable BH mass from broad Hα. We thus very aggressively flag all suspicious objects based on their line strength, by applying a combined cut on total Hα flux normalized to the rms deviations in the continuum-subtracted spectrum, and the Hα equivalent width (EW). We require that $f_{H\alpha}$/rms > 200 and EW(Hα) > 15 Å. The EW measurement is based on continuum measured from the best-fit PCA galaxy model in the spectral regions 6570–6590 Å and 6480–6540 Å. In detail, our thresholds are selected based on simulations, presented in Appendix A, which demonstrate that for the S/N ratios typical in the SDSS, BH mass estimates are highly uncertain (> 1 dex) and significantly biased for lower Hα fluxes and EWs. Hereafter, this combination of cuts will be referred to as the "detection threshold." Following the automated flagging, some objects at the low-mass end are still questionable when examined by eye. They are flagged as well. A total of 11,428 objects are removed at this stage. For comparison with previous work, we also build a more inclusive luminosity function that does not reject the flagged objects.

There are a number of scientifically interesting objects that fall below the detection threshold. There are strongly star-forming galaxies with a broad Hα base (see also Hao et al. 2005a) that are probably Wolf-Rayet galaxies (Ho et al. 1997c). In other cases, we are probably seeing a small, scattered component of broad emission in what is predominantly a narrow-line AGN. In this case, the Hα luminosity does not correlate with the broad-line region size. Finally, if the BH is radiating at a very low fraction of its Eddington luminosity then it is thought that the standard optically thick, geometrically thin accretion disk (Shakura & Sunyaev 1973) is replaced by a radiatively inefficient accretion mode (e.g., Quataert 2001; Narayan 2006 and references therein). Although no such objects are included in the reverberation-mapped samples used to calibrate the radius-luminosity relation (e.g., Kaspi et al. 2005) it is likely that the broad-line region structure is quite different in this regime. While we do not have sufficient S/N in single objects to accurately measure BH masses, it is quite possible that in stacked spectra we would be able to uncover very low-contrast

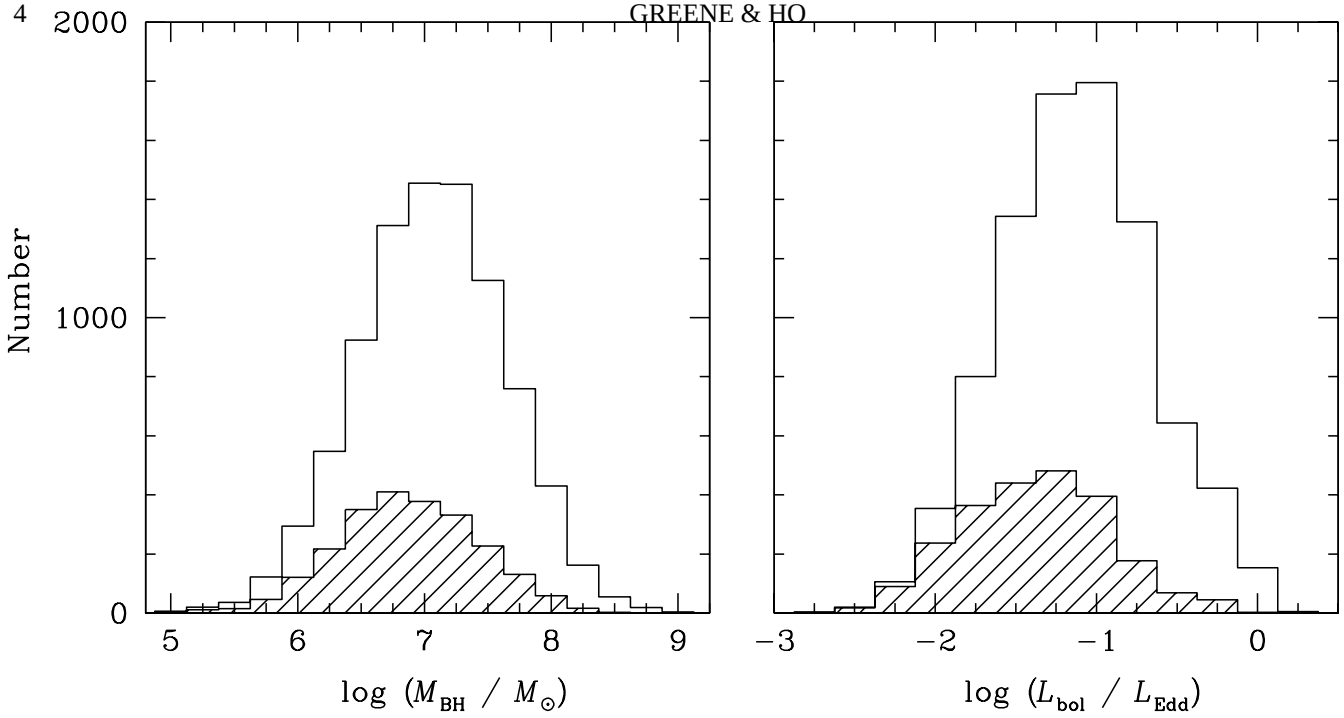

FIG. 2.— Distributions of BH mass (*left*) and $L_{\rm bol}/L_{\rm Edd}$ (*right*) for the entire sample of broad-line AGNs. $M_{\rm BH}$ is calculated from $L_{\rm H\alpha}$ and FWHM$_{\rm H\alpha}$ as shown above, using the formalism of Greene & Ho (2005b), and the Eddington ratio is derived assuming an average bolometric correction of $L_{\rm bol} = 2.34 \times 10^{44} (L_{\rm H\alpha}/10^{42})^{0.86}$ ergs s^{-1} (see text). As in the previous figure, the galaxies targeted in the SDSS main sample are indicated with the shaded histogram. Note that while the galaxy-selected AGNs are uniformly at low luminosities, they span the entire range of $M_{\rm BH}$ in the sample. Massive BHs are predominantly in low-accretion states at the present time.

broad lines. We defer such analysis to a later work.

Finally, we note that narrow-line AGN samples are typically selected using their location in diagnostic diagrams (Baldwin et al. 1981; Veilleux & Osterbrock 1987; Ho et al. 1997a; Kauffmann et al. 2003; Hao et al. 2005a) that discriminate the shape of the ionizing continuum by the relative strengths of various prominent narrow emission lines. Our selection technique relies on the presence of broad emission lines, and so is unbiased with respect to line ratios. This is particularly useful for selecting relatively metal-poor AGN hosts, since the typically high ratio of [N II]/Hα may be significantly reduced. This has been observed in NGC 4395 (e.g., Kraemer et al. 1999), with low significance in the original Greene & Ho (2004) sample, and quite strikingly in our new sample of Type 2 low-mass BHs (A. J. Barth et al., in preparation; see also Groves et al. 2006). In contrast to standard narrow-line selections, therefore, our selection is relatively unbiased against AGNs in low-metallicity (and thus typically low-mass; e.g., Tremonti et al. 2004) galaxies in this manner.

Our final sample (with duplicates removed) of broad-line AGNs is composed of 8728 objects. The Princeton spectral reductions include single-Gaussian fits to narrow emission lines, and flags for all objects with an additional broad component. Approximately 30% of the broad-line objects in their sample are rejected by our algorithms, some (35%) with the initial Hα-finding algorithm, and the rest either because of a lack of broad Hα in the multi-Gaussian fit, or because they fall below our detection threshold. We have examined a large number of these objects visually, and we feel justified in rejecting them. One contaminant in particular consists of objects with multi-component narrow lines, which confuse algorithms that fit only single Gaussians to the narrow lines. We also compare with the Hao et al. (2005a) list of broad-line AGNs. Only 53% of their broad-line sample is included in our final sample; 17% are rejected by our initial broad-line search algorithm, 11% are deemed to have no broad Hα in more detailed fitting, and 19% are rejected by our detection threshold.

We have measured the Hα luminosities (with no internal reddening correction applied) and FWHM$_{\rm H\alpha}$ for our entire sample of broad-line AGNs (Fig. 1). The FWHM$_{\rm H\alpha}$ are measured from the multi-component Gaussian models (as in Greene & Ho 2004). We can use these measured quantities and the formalism presented in Greene & Ho (2005b) to derive BH masses for the sample. We also use the measured Hα luminosities and the inferred BH masses to estimate Eddington ratios for the sample, $L_{\rm bol}/L_{\rm Edd}$, where $L_{\rm Edd} \equiv 1.26 \times 10^{38}$ $(M_{\rm BH}/M_\odot)$ ergs s^{-1}. Assuming that $L_{\rm bol} = 9.8\ L_{5100}$ (McLure & Dunlop 2004), in terms of $L_{\rm H\alpha}$ our bolometric correction is $L_{\rm bol} = 2.34 \times 10^{44} (L_{\rm H\alpha}/10^{42})^{0.86}$ ergs s^{-1} (Greene & Ho 2005b). We adopt this bolometric correction throughout. The corresponding distribution of BH masses and Eddington ratios is shown in Figure 2. At face value the mass function is strongly peaked at $10^7\ M_\odot$, while the typical Eddington ratio of our sample is about a tenth of the Eddington limit. However, there are severe selection effects that cause us to lose significant numbers of sources, and these depend on mass, Eddington ratio, and redshift. The strong importance of selection effects is shown in Figure 3, where the distribution of BH mass in the sample is shown as a function of both redshift and Eddington ratio. The most striking trends in this figure are the decrease of characteristic BH mass as one moves to higher Eddington ratio at a given redshift, and the increase of characteristic mass as one moves to higher redshift at a given Eddington ratio. Both of these trends are driven by the magnitude limits of the SDSS.

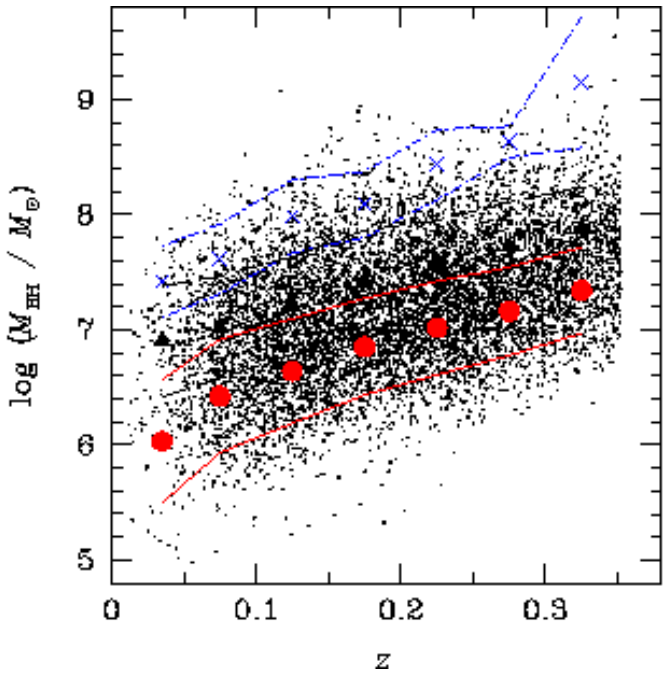

FIG. 3.— Distribution of $M_{\rm BH}$ with redshift is shown in small points for the entire sample. In large symbols we represent the mean mass in three different Eddington ratio bins, with 1 σ contors bracketing each bin. The blue crosses and dash-dotted lines show objects with $L_{\rm bol}/L_{\rm Edd} < 0.01$, the black triangles and dashed lines show $0.01 < L_{\rm bol}/L_{\rm Edd} < 0.1$, and the red circles and solid lines are objects with $L_{\rm bol}/L_{\rm Edd} > 0.1$.

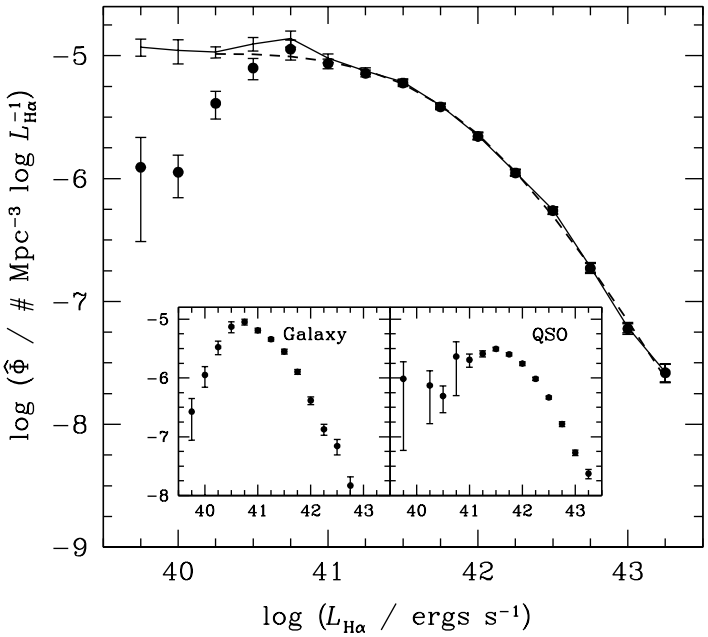

FIG. 4.— Volume-weighted broad Hα luminosity function in bins of 0.25 dex (# Mpc^{-3} log $L_{\rm H\alpha}{}^{-1}$). The maximum volume is calculated based on both the photometric and spectroscopic limits of the survey and our search algorithm (see text). The error-bars represent the Poisson errors in each bin. The solid line represents our maximally inclusive sample, in which objects with less reliable broad Hα are included. Our best-fit double power law is shown as the dashed line. The inset panels show the luminosity functions for objects targeted as galaxies or AGNs, respectively, primarily based on a color selection.

4. LUMINOSITY AND MASS FUNCTIONS

4.1. *Broad Hα Luminosity Function*

We begin by calculating a traditional luminosity function $\Phi(L_{\rm H\alpha})$ for our broad-line active galaxy sample. While the luminosity function is difficult to interpret directly, in so far as it is a convolution of the BH mass and Eddington ratio distributions, nevertheless it has the benefit of being a directly observable quantity. BH masses, on the other hand, are potentially subject to considerable systematic uncertainties (e.g., Greene & Ho 2006b; Collin et al. 2006). Furthermore, the luminosity function is readily compared with various probes of the active galaxy population, such as the X-ray luminosity function for AGNs. Following common practice, we present the differential luminosity function, the number of AGNs per unit volume per logarithmic luminosity interval, $\hat{\Phi}(L_{\rm H\alpha}) = (L_{\rm H\alpha}/\log_{10}e)\Phi(L_{\rm H\alpha})$. Since galaxies of different magnitude are observable to varying distance within the sample, a proper representation of the distribution of AGN luminosity (or mass) requires that we somehow account for our variable sensitivity prior to comparing their distributions directly. We primarily use the classical $V/V_{\rm max}$ weighting method (Schmidt 1968; Huchra & Sargent 1973; Condon 1989; Ulvestad & Ho 2001), but in Appendix B we present a non-parametric maximum likelihood luminosity function as well (e.g., Efstathiou et al. 1988).

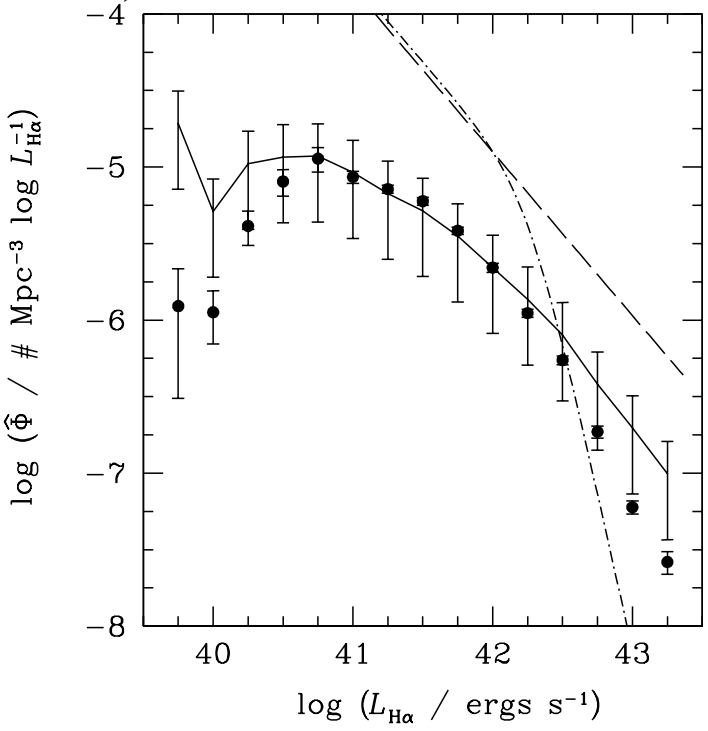

FIG. 5.— Broad Hα luminosity function calculated using the maximum likelihood formalism (solid line; see Appendix B for details). The $V/V_{\rm max}$ luminosity function is shown in solid symbols as in Figure 4. Also shown are the single (dashed line) and double (dot-dashed line) power-law fits to the Hao et al. (2005b) maximum likelihood total Hα luminosity function.

In the $V/V_{\rm max}$ formalism, our sensitivity is characterized as the maximum volume to which each source would be included in our final sample. In calculating $V_{\rm max}$, we must account for both the magnitude limit of the SDSS and the S/N dependence of our Hα detection procedure. The appropriate magnitude limit will depend on whether a given object was targeted as a galaxy or quasi-stellar object (QSO). The main galaxy sample comprises spatially resolved (i.e., non-stellar) targets above a limiting r-band Petrosian magnitude of 17.77 mag (Strauss et

al. 2002). QSO targets, in contrast, are selected with a rather complicated set of color-selection criteria within a magnitude range of $15.0 < i < 19.1$ (Richards et al. 2002; Stoughton et al. 2002). The maximum flux limit mitigates bleeding between fibers. A different color criterion is used to select high-redshift QSO candidates, and these have a limiting magnitude of $i = 20.2$; a small number (237) of our final targets fall into this category. We note that it is possible for objects to have been targeted as either a QSO or a galaxy; these objects are considered part of the galaxy sample. Now, in addition to these two primary surveys, some "serendipitous" sources are targeted, due to a detection either in the *ROSAT* All-Sky Survey (Voges et al. 1999), or by the FIRST radio survey (Becker et al. 1995; see also Richards et al. 2002). We have 154 such objects; they do not constitute a complete sample, nor do they have a uniform detection limit. We therefore assign them a maximum volume corresponding to their observed volume (i.e., take $V_{\rm max} = V$), and then verify that our conclusions are unchanged when we exclude them from the sample.

Table 2. Broad Hα Luminosity Function

log ($L_{\rm H\alpha}$) (1)	log $\hat{\Phi}$ (2)
39.75	$-5.91^{+0.24}_{-0.60}$
40.00	$-5.95^{+0.14}_{-0.21}$
40.25	$-5.39^{+0.10}_{-0.13}$
40.50	$-5.10^{+0.08}_{-0.10}$
40.75	$-4.95^{+0.07}_{-0.09}$
41.00	$-5.06^{+0.04}_{-0.04}$
41.25	$-5.14^{+0.03}_{-0.03}$
41.50	$-5.22^{+0.02}_{-0.03}$
41.75	$-5.42^{+0.02}_{-0.02}$
42.00	$-5.66^{+0.03}_{-0.03}$
42.25	$-5.95^{+0.03}_{-0.03}$
42.50	$-6.26^{+0.03}_{-0.03}$
42.75	$-6.73^{+0.04}_{-0.04}$
43.00	$-7.22^{+0.04}_{-0.04}$
43.25	$-7.58^{+0.07}_{-0.08}$

Note. — Col. (1): Log $L_{\rm H\alpha}$ (ergs s^{-1}). Col. (2): Space density (# Mpc^{-3} log $L_{\rm H\alpha}{}^{-1}$) as a function of broad Hα luminosity.

Based on the target selection of each object, it is straightforward to calculate the maximum volume to which the SDSS would have spectroscopically targeted a given object, with approximate k-corrections based on the observed colors. In detail, of course, the color (and thus target selection) of a source is redshift-dependent, as the spatially resolved galaxy light will dim more rapidly than the unresolved AGN light. This is difficult to model without a good separation of host and AGN light. Nevertheless, since the majority of the galaxy targets are very close to their limiting magnitude, this should not affect the results in practice.

With increasing redshift and commensurately degraded S/N, it becomes more and more challenging to detect broad Hα. At a certain point, the object reaches our imposed detectability threshold, and is removed from the sample. In detail, however, our algorithm may lose the ability to detect the object even before this limit is reached. This depends on the contrast of the broad line, the galaxy subtraction, the strength of the narrow lines, etc. In principle, it is also possible that the galaxy dilution increases as the physical radius subtended by the fixed SDSS fiber increases, although it will be mitigated to some degree by surface brightness dimming, and we have neglected this effect. To model our incompleteness, we generate artificial spectra over a grid of redshifts (S/N) between the observed redshift and either the photometric redshift limit or the detectability threshold redshift, whichever is smaller. The S/N at each interval is calculated based on the fiber magnitude of the source at the new redshift and an empirical relation between fiber magnitude and S/N we have derived from the SDSS data. If the interval is smaller than $\delta z = 0.05$, we simply bisect the redshift interval, whereas for larger redshift ranges we generate artificial spectra at $z_{\rm max} - 0.05$ and the center of the redshift interval. We generate three spectra at each redshift, with a range of S/N $\pm$20% of the calculated value. When the calculated S/N is ≤ 5, the limiting redshift is automatically reached, as such spectra are simply unusable. We subject the remaining spectra to our full selection algorithm. As long as two of the three artificial spectra are recognized as broad-line AGNs, we continue to the next redshift bin. In practice, only $\sim 20\%$ of our $V_{\rm max}$ calculations are lowered by these simulations, suggesting that our detection threshold is reasonable.

Using the $V/V_{\rm max}$ weights derived above, the luminosity function ($\hat{\Phi}$) and uncertainty per bin (σ) are simply calculated:

$$\hat{\Phi}(L_{\rm H\alpha}) = \sum_i^N \left(\frac{1}{V_{\rm max}}\right)_i, \sigma = \left[\sum_i^N \left(\frac{1}{V_{\rm max}}\right)_i^2\right]^{1/2}; \quad (1)$$

they are shown in Table 2 and Figure 4. The survey volume is determined assuming an angular coverage of 4783 deg^2 of the DR4 spectroscopic survey[2]. We compute the number of AGNs per unit volume, per unit logarithmic luminosity [$\hat{\Phi}(L_{\rm H\alpha})$] in bins of 0.25 dex in Hα luminosity, from $10^{40} - 10^{43.25}$ ergs s^{-1}. In the insets are plotted the luminosity functions for objects targeted as galaxies (*left*) and QSOs (*right*). The "galaxies" are strongly peaked at the luminosity of a 10^7 $M_\odot$ BH radiating at 10% of Eddington. At higher luminosity, the QSOs tend to dominate the light, while at the lowest luminosities, there are equal numbers of each type, depending on whether the source is a low-mass BH at higher Eddington ratio (QSO) or a more massive and less active source. Note that the decline at luminosities below $\lesssim 10^{40.75}$ ergs s^{-1} is due to incompleteness. For instance, the Palomar spectroscopic survey of nearby galaxies, with significantly higher sensitivity to low-level broad emission, finds a luminosity function that continues to rise to significantly lower luminosities (Ulvestad & Ho 2001; Ho 2004). For this reason, we also calculate a maximally inclusive luminosity function, retaining all flagged objects. That is shown as a solid line in Figure 4.

[2] http://www.sdss.org/dr4/

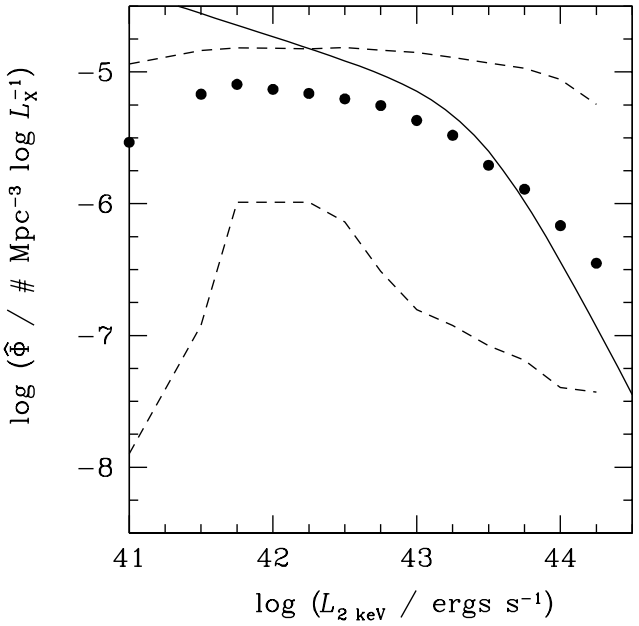

FIG. 6.— Conversion of our observed luminosity function to an X-ray luminosity function using the Strateva et al. (2005) relation between UV luminosity and α_{ox}. Solid line is the soft X-ray, unabsorbed luminosity function presented in Hasinger et al. (2005). The points represent the median luminosity function of 1000 Monte Carlo realizations of the optical to X-ray conversions, which account for its significant scatter. The dotted lines bracket 68% of the resulting distribution in a given luminosity bin.

For comparison with other samples it is useful to parameterize the observed luminosity function. Following previous work, we consider a Schechter (1976) function and a double power law (e.g., Croom et al. 2004; Hao et al. 2005b),

$$\phi(L) = \frac{\phi^*(L_*)/L_*}{(L/L_*)^{\alpha}+(L/L_*)^{\beta}}, \quad (2)$$

where $\phi^*(L_*)$, L_*, α and β are free parameters. We use a χ^2 minimization fitting procedure that accounts for the asymmetric errors in space density, and we fit all objects in our final sample with luminosities $\geq 10^{40}$ ergs s^{-1} (for this luminosity range the results do not change if we fit the inclusive sample). The Schechter fit has a reduced χ^2_r= 11, while the double power-law fit has a reduced χ^2_r= 1.3. Therefore, we prefer the latter, which yields values of $\phi(L_*) = (2.0 \pm 0.4) \times 10^{-6}$ Mpc^{-3}, $L_* = 10^{42.0\pm0.1}$ ergs s^{-1}, $\alpha = 1.29 \pm 0.09$, and $\beta = 2.82 \pm 0.07$. This fit is shown as a dashed line in Figure 4.

4.2. *Comparison with Hao et al. (2005b)*

Hao et al. (2005b) used a smaller subsample of the SDSS to compute emission-line luminosity functions for broad- and narrow-line AGNs. They used very comparable selection criteria to select their broad-line subsample, and thus it is important to compare our results with theirs. In order to compare directly with their work we construct an additional luminosity function using the maximum likelihood formalism (for details, see Appendix B). At high luminosity, Hao et al. have limited statistics (as demonstrated by the divergence of their single and double power-law fits in Fig. 5), but the double power-law fit does provide a better fit to their highest luminosity bins, consistent with our result. At lower luminosity, our function diverges from that of Hao et al. We believe this discrepancy may be attributed to three factors.

Firstly, we consider flux only from broad Hα, while Hao et al. include both narrow and broad emission. This has no effect at high luminosity, where the narrow-line luminosity constitutes a negligible fraction of the total, but at lower luminosities, objects with high-EW narrow lines will be preferentially shifted into higher luminosity bins in the Hao et al. function. Secondly, we remove a large number of broad-line AGNs below our detection threshold. However, even when we include these objects, our luminosity function flattens at considerably higher luminosity than the Hao et al. function. Relative to Hao et al. we have removed objects both with our initial Hα detection algorithm and with our line-fitting procedure, at the $\sim$ 20% level. Because the luminosities involved are very low, the corresponding volume corrections are very large, leading to highly discrepant space densities in the two studies. In some respects it is not surprising to find such a large range of possible space densities at these very low Hα luminosities. As we show in Appendix A, the measurements of $L_{H\alpha}$ are very inaccurate in this regime. Perhaps the most important message of this exercise is that the SDSS is not an adequate tool to measure the line luminosity function below $\sim 10^{40.5}$ ergs s^{-1}.

In addition to the differences in object selection, we adopt a very different set of assumptions in building our luminosity functions than Hao et al. They have used the maximum likelihood formalism, but in calculating their selection function [$p_i(L)$] have assumed that neither the line shape nor the galaxy luminosity are linked to the Hα luminosity. In our V/V_{max} formalism, we need not make any assumption about galaxy luminosity. However, when we calculate our selection function for the maximum likelihood function, we do not allow a given object to exceed its Eddington luminosity, thus implicitly assuming a correlation between galaxy and AGN luminosity. For the majority of objects, we are thus adopting a higher maximum luminosity than the fiducial luminosity of $\sim 10^{42.6}$ ergs s^{-1} assumed by Hao et al.. Furthermore, we assume that as the AGN luminosity decreases for a given object, the line width increases, thus increasing the noise per pixel across the broad line, and decreasing our detection efficiency at low luminosity. The net effect at low luminosity is apparently that we have larger volume corrections than Hao et al., leading to lower inferred space densities.

As an aside, we note that our luminosity function is consistent with that of Croom et al. (2004), with the break luminosity $\sim$ 1 mag lower. On the other hand, while the Hao et al. function appears to be consistent with that of Ulvestad & Ho (2001; see Fig. 11 of Hao et al.), the galaxy luminosity is included in the latter luminosity function. In most cases the AGN luminosity itself is significantly fainter, and it is probably fair to shift their function fainter by $\sim$ 4 magnitudes (see Ho 2004 for details).

4.3. *X-ray Luminosity Function*

As an additional sanity check, we compare our luminosity function with the zero-redshift luminosity functions presented by Hasinger et al. (2005). This work focuses predominantly on soft X-ray–selected samples with broad Balmer lines in optical follow-up (see also Schmidt et al. 1998). To perform a comparison, we (statistically) convert our observed Hα luminosities to soft X-ray luminosities. We employ the Greene & Ho (2005b) conversion between Hα luminosity and L_{5100}, and then, assuming a spectral slope of $\alpha = 0.44$ ($f_\nu \propto \nu^{-\alpha}$; see, e.g., Vanden Berk et al. 2001; Greene & Ho 2005b), the relation between α_{ox} and L_{2500} from Strateva et al. (2005). Although the Strateva et al. relation (see also Steffen et al. 2006) is only measured for UV luminosities of $\sim 10^{43}-10^{48}$ ergs s^{-1}, Greene

& Ho (2007) find that, in general, the low-mass AGNs from Greene & Ho (2004) obey the extrapolation of the Strateva relation to lower luminosity. Because there is large scatter in the conversion between X-ray and optical luminosity, we generate 1000 X-ray luminosity functions from our optical function, in each case perturbing the intercept and slope of the relation by a log-normal deviate determined by the measured scatter in each variable. We then select the median value at each luminosity, and the upper and lower bounds to bracket 68%. The resulting inferred soft X-ray luminosity function is shown in Figure 6, with the Hasinger et al. double power-law fit shown as a solid line. Given the uncertainties involved, we find quite reasonable agreement.

Table 3. BH Mass Function

log ($M_{\rm BH}$) (1)	log ($\hat{\Phi}$) (2)
5.00	$-6.10^{+0.16}_{-0.25}$
5.25	$-5.81^{+0.17}_{-0.27}$
5.50	$-6.05^{+0.11}_{-0.14}$
5.75	$-5.51^{+0.07}_{-0.08}$
6.00	$-5.21^{+0.08}_{-0.09}$
6.25	$-5.06^{+0.10}_{-0.13}$
6.50	$-5.13^{+0.05}_{-0.05}$
6.75	$-5.10^{+0.04}_{-0.04}$
7.00	$-5.10^{+0.05}_{-0.05}$
7.25	$-5.31^{+0.03}_{-0.03}$
7.50	$-5.50^{+0.06}_{-0.07}$
7.75	$-5.79^{+0.06}_{-0.07}$
8.00	$-6.22^{+0.05}_{-0.06}$
8.25	$-6.82^{+0.05}_{-0.06}$
8.50	$-7.32^{+0.09}_{-0.11}$
8.75	$-7.98^{+0.11}_{-0.14}$

Note. — Col. (1): Virial $M_{\rm BH}$ ($M_\odot$) as inferred from $L_{\rm H\alpha}$ and FWHM$_{\rm H\alpha}$. Col. (2): Space density (# Mpc^{-3} log $M_{\rm BH}{}^{-1}$) as a function of $M_{\rm BH}$.

4.4. *BH Mass Function*

Using the $V_{\rm max}$ weights derived above, we show in Figure 7 volume-weighted BH mass function (the number of BHs per unit volume, per unit logarithmic BH mass, in bins of 0.25 dex in BH mass; see also Table 3). As with the luminosity function, we fit the mass function with a Schechter function, a double power law, and a log-normal parameterization. In this case we include all mass bins in the fitting. Once again, the Schechter function provides a poor fit, with χ^2_r = 18. Both the double power-law and log-normal functions provide reasonable fits, with χ^2_r = 2.5 and χ^2_r = 1.2, respectively. The best-fit double power law is shown as a dashed line in Figure 7, and is parameterized by $\phi(M_*) = (4.7 \pm 0.5) \times 10^{-6}$ Mpc^{-3}, $M_* = 10^{7.32\pm0.05}$ $M_\odot$, $\alpha = 0.78 \pm 0.06$, and $\beta = 3.00 \pm 0.07$. The log-normal fit, shown as a solid line in Figure 7, has a normalization of $(6.4 \pm 0.3) \times 10^{-6}$ Mpc^{-3}, a central mass of $10^{6.6\pm0.03}$ $M_\odot$, and a width of 0.59 ± 0.01 dex.

Taken at face value, our BH mass function displays a clear break at $\sim 10^{6.6}$ $M_\odot$, and declines toward both higher and lower mass. This is comparable to the characteristic mass of local narrow-line AGNs (Heckman et al. 2004) but is significantly lower than that of inactive BHs ($\sim 10^8$ $M_\odot$; e.g., Marconi et al. 2004). Unfortunately, as demonstrated by Figure 3, our data are dominated by the strong selection bias inherent in a magnitude-limited sample. It is clear that, in terms of luminosity, we are significantly incomplete below $\sim 10^{40.75}$ ergs s^{-1}. However, incompleteness in luminosity is redshift-dependent and may not be translated directly into incompleteness as a function of BH mass. At a given $L_{\rm H\alpha}$, the S/N across the line (and thus its detectability) decreases with increasing FWHM$_{\rm H\alpha}$, and thus increasing BH mass. Additionally, as the BH mass increases, the corresponding bulge luminosity is presumably increasing, further decreasing the contrast and the S/N in the broad line.

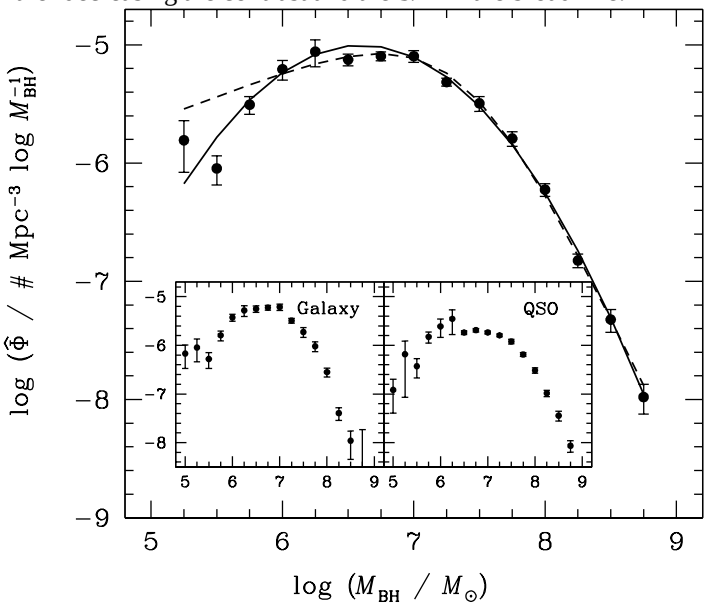

FIG. 7.— Volume-weighted BH mass function in bins of 0.25 dex (# Mpc^{-3} log $M_{\rm BH}{}^{-1}$). The weights used are identical to those for the luminosity function, and as above we show in the inset the mass functions for objects targeted as galaxies (*left*) and QSOs (*right*), respectively. Although we are subject to significant incompleteness, we will argue below that there is truly a turnover in active galaxy masses at both lower and higher BH masses. We have fit the mass function with both a double power-law (dashed line) and a log-normal function (solid line).

If we could uniquely ascribe a host galaxy luminosity and light profile to each $M_{\rm BH}$, then we could easily model our incompleteness as a function of $M_{\rm BH}$ and $L_{\rm bol}/L_{\rm Edd}$. At high BH mass, this is in fact possible, as there is a relation linking $M_{\rm BH}$ and spheroid luminosity, and the fundamental plane tells us the typical sizes (and thus fiber luminosities) of elliptical galaxies. However, for spiral or dwarf spheroidal host galaxies, there ceases to be a unique mapping between $M_{\rm BH}$ and galaxy luminosity or structure. The relation between bulge-to-total ratio and galaxy luminosity is poorly quantified and contains significant scatter in any case. Furthermore, at lower masses, as the AGNs become intrinsically fainter, only systems with relatively luminous host galaxies will fall above the magnitude limit of the SDSS. For these reasons, at low $M_{\rm BH}$ the calculated incompleteness is a strong function of the assumed (but unconstrained) host galaxy morphology.

As a matter of practicality, then, we turn the problem around. Rather than attempting to quantify our absolute incompleteness as a function of $M_{\rm BH}$, we simply quantify the range of host galaxy luminosities for which we might hope to detect a BH of a given mass, $L_{\rm H\alpha}$, and z. Over narrow ranges in all of these parameters, neither the line width nor the galaxy contin-

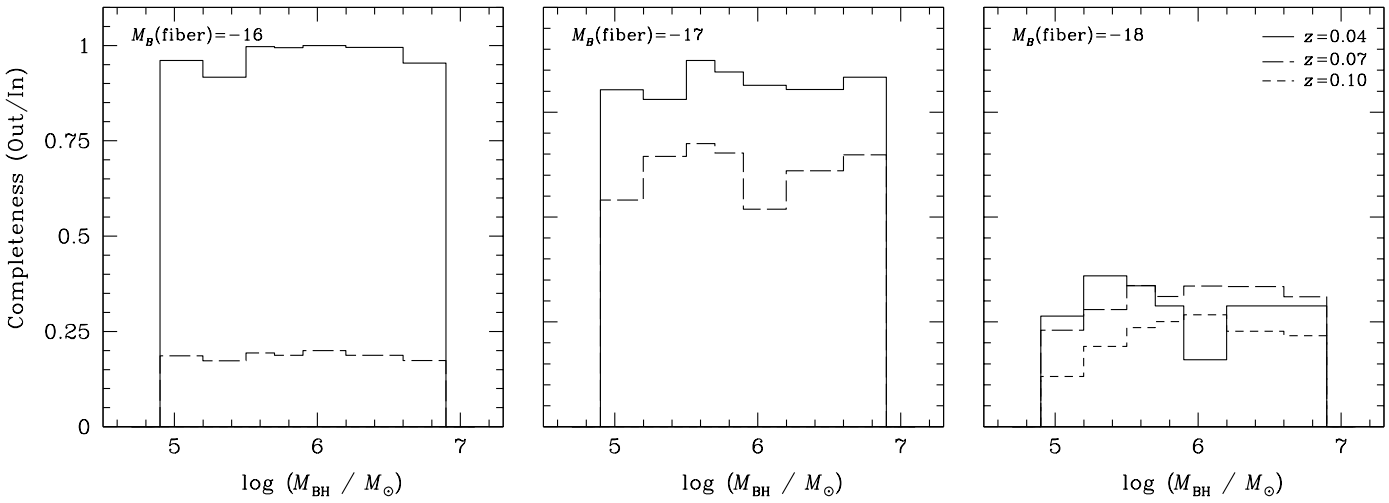

FIG. 8.— Incompleteness as a function of galaxy luminosity for simulated galaxies. These simulations are run for BH masses of $M_{\rm BH}$= $10^{5.5}-10^{6.4}$ $M_\odot$ at three redshifts (z = 0.04, 0.07, 0.10), and with the limited range of $L_{\rm H\alpha}$= $10^{40.5}-10^{41}$ ergs s^{-1}. Although the input fiber luminosities are $-14 \leq M_B \leq -22$, there are non-zero detection fractions only over the range of fiber luminosities shown here. The simulations demonstrate that we have roughly constant incompleteness over this range in $M_{\rm BH}$, $L_{\rm H\alpha}$, and z.

uum strength changes dramatically and the completeness ought to be constant (provided the BHs are drawn from the same host galaxy population). In such bins, with uniform completeness, we are able to measure true changes in space density. Simulations allow us to isolate ranges of $M_{\rm BH}$, $L_{\rm H\alpha}$, and z with constant sensitivity to galaxy fiber luminosity. Note, however, that in any given interval, we necessarily exclude different members of the population as a function of $M_{\rm BH}$; at the lowest masses we preferentially exclude those systems in faint hosts, while at the highest $M_{\rm BH}$ we exclude the higher $L_{\rm bol}/L_{\rm Edd}$ systems. Therefore, we implicitly assume that the distribution of $M_{\rm BH}$ is uniform independent of both disk luminosity and Eddington luminosity. With this approach, however, we need not concern ourselves directly with host galaxy structure[3] per se, but solely the luminosity. The total host galaxy luminosity must be high enough that the source is spectroscopically targeted, while the fiber luminosity must be low enough to allow detection of the broad line.

We investigate three mass regimes ($M_{\rm BH}$=$10^{5.5}-10^{6.4}$, $10^{6}-10^{7}$, and $10^{6.5}-10^{7.5}$ $M_\odot$), choosing optimal z and $L_{\rm H\alpha}$ ranges for each. Our procedure is described in most detail for the lowest (and most challenging) mass bin, and then results are presented for all three. In the first bin, we are fundamentally limited by the total number of objects. Therefore, we are forced to use the lowest possible redshift bins: $z = 0.05-0.07$ and $z = 0.07-0.1$. These are bins with ≥ 10 objects per bin for the most part; at still lower z a prohibitively large range in distance is needed to populate each bin. In terms of $L_{\rm H\alpha}$, the highest luminosity is set by the Eddington luminosity of the lowest mass bin, in this case 10^{41} ergs s^{-1} for a BH with mass $10^{5.5}$ $M_\odot$, while the lowest luminosity is set by the paucity of lower-luminosity objects ($10^{40.5}$ ergs s^{-1}).

Simulations allow us to verify that the selection probability is indeed independent of host galaxy fiber luminosity. We make artificial spectra in the appropriate $M_{\rm BH}$ and $L_{\rm H\alpha}$ range, with fiber galaxy luminosities spanning $-14 \leq M_B \leq -22$. The galaxy continuum is modeled as a single stellar absorption-line system, constructed from the eigenspectra of Yip et al. (2004), and the S/N is varied to correspond to typical SDSS spectra over the redshift range of interest. Five realizations are made for each galaxy luminosity and S/N, and each spectrum is run through our full detection algorithm. For those with detectable broad Hα, we then investigate whether the galaxy luminosity is sufficient for spectroscopic targeting in the first place. Recall that this limit depends on total (rather than fiber) luminosity, but there is not a one-to-one conversion from fiber to total luminosity; it depends on galaxy morphology and redshift rather strongly. Therefore, we place an upper limit on the total galaxy luminosity by insisting that the fiber luminosity account for no less than 20% of the total galaxy luminosity (as motivated by the observed range shown in Fig. 9 of Tremonti et al. 2004). Over the entire range of galaxy luminosities we explore, a non-zero detection fraction results only for fiber luminosities in the range $-16 < M_B < -18$, but the detection fractions at a given host luminosity are very constant across the mass range of interest, as shown in Figure 8.

In Figure 9*a* we show the resulting mass functions for the two different redshift bins. Visually, it appears that the space density is truly falling at low mass. To quantify the significance of this result, we perform a simultaneous fit to the mass functions in the two redshift bins. We have chosen to use a single power-law in this case,

$$\phi = \frac{\phi^*(M_*)}{M_*}\left(\frac{M}{M_*}\right)^{\alpha}. \quad (3)$$

The two redshift bins are constrained to have the same value of α but are allowed different values of $\phi^*(M_*)$. An apparent flat slope in our logarithmic mass function, $\hat{\Phi}(M_{\rm BH})$, would correspond to $\alpha = -1$. We find a reduced χ^2_r=1.01 and a best-fit slope of $\alpha = -0.6 \pm 0.2$, corresponding to a 2 σ detection of a falling space density for $M_{\rm BH} \lesssim 10^{6.5}$ $M_\odot$. If we relax the luminosity criterion to include all objects with $L_{\rm H\alpha}$ = $10^{40}-10^{41}$ ergs s^{-1}, the best-fit slope is $\alpha = -0.7 \pm 0.1$. We have performed this fit including the lowest-mass point ($M_{\rm BH}$= $10^{5.2}-10^{5.5}$ $M_\odot$), but this point is suspect both because there only 5 objects in the bin, and also because our maximum $L_{\rm H\alpha}$ exceeds the Eddington limit for BHs in this bin. However, when this point is removed, the best-fit slope does not change. The major out-

[3] At a given luminosity, a wide range of galaxy morphologies are permitted. Thus it is still possible to find significant differences in σ_* (e.g., Greene & Ho 2006b) and potentially host galaxy structure (J. E. Greene, in preparation) as a function of $M_{\rm BH}$ for the SDSS-selected samples of low-mass systems.

standing caveats, unavoidable products of our technique, are that these BHs must both be highly active and live in fairly luminous host galaxies.

We repeat the above analysis for two other mass intervals. For the first, $M_{\rm BH} = 10^6 - 10^7\ M_\odot$, we employ a luminosity interval of $L_{\rm H\alpha} = 10^{40.5} - 10^{41.7}$ ergs s^{-1} and, because there are many more objects in this mass range, three redshift intervals, $z = 0.05-0.08$, $0.08-0.11$, and $0.11-0.14$. The fitting results are shown in Figure 9*b*, and, with a best-fit $\alpha = -0.72 \pm 0.06$, are consistent with the slope found above. In this case, we have a 5 σ detection of decreasing space density below $M_{\rm BH} < 10^7\ M_\odot$. However, it should be noted that the best fit has $\chi^2_r = 2.7$, suggesting that this is not a terribly good model. While we might achieve an improved fit with a broken power-law model, this hardly seems justified for such a limited range in BH mass. Finally, we turn to the break at high mass, using the mass bin $M_{\rm BH} = 10^{6.5} - 10^{7.5}\ M_\odot$, and the luminosity bin $L_{\rm H\alpha} = 10^{41} - 10^{42}$ ergs s^{-1}. Again we are able to utilize three redshift bins. Because of the bright magnitude limit of the SDSS, we are forced to go to higher redshift for completeness in the highest mass bins here, $z = 0.10-0.13$, $0.13-0.16$, and $0.16-0.19$. In this mass bin, the mass function begins to turn over: we find a best-fit $\alpha = -1.13 \pm 0.04$, corresponding to a 3 σ detection of a falling space density above $M_{\rm BH} \gtrsim 10^{6.5}\ M_\odot$. Again, the single power-law model is not a fantastic fit (χ^2_r=3.4), so it is difficult to say when the turnover actually occurs. If we repeat the fit without the highest mass bin, the fit apparently improves ($\chi^2_r = 1.6$) and the slope steepens, $\alpha = -1.40 \pm 0.05$. Even if we neglect the top two or three mass bins, we find the same result. Therefore, we cannot exactly localize the break; it occurs somewhere in the range $10^{6.5} - 10^{7.5}\ M_\odot$.

4.5. *Comparison with Heckman et al. (2004)*

For the first time, we are able to compare narrow- and broad-line AGN mass functions rather than just luminosity functions (Fig. 10). The narrow-line objects come from the SDSS database of Kauffmann et al. (2003), for which BH masses are inferred from the stellar velocity dispersion (Heckman et al. 2004; we actually use the most recent sample from DR4). Reliable BH masses extend no lower than $10^{6.3}\ M_\odot$ due to the resolution limit of the SDSS ($\sigma \approx 71$ km s^{-1}; e.g., Heckman et al. 2004). Volume weights depend only on galaxy luminosity, since they were selected from the main galaxy sample.

It is clear that the space density of narrow-line AGNs in the Heckman et al. sample is higher than that of the broad-line sample by an order of magnitude. However, it is crucial to remember that the selection effects for the two samples are radically different. In particular, narrow emission lines may be detected to significantly lower luminosities than broad lines. Therefore, while the typical Eddington ratio in our sample is $L_{\rm bol}/L_{\rm Edd} \approx 0.1$, the typical $L_{\rm bol}/L_{\rm Edd}$ for a $10^7\ M_\odot$ BH in the Heckman et al. sample is closer to $L_{\rm bol}/L_{\rm Edd} \approx 0.04$ (see their Fig. 3). It would be much more informative to compare the broad- and narrow-line objects in matching mass and luminosity bins. However, to do so properly requires a consistent measure of AGN luminosity across the two samples. Typically, the [O III] line is used (e.g., Zakamska et al. 2003), but for broad-line objects there may be significant contamination to this line from broad Fe II emission (e.g., Greene & Ho 2005b). Since we have not properly subtracted the Fe II, a more detailed comparison must await future work.

5. DISCUSSION

5.1. *Active Fraction or Duty Cycle*

We have constructed a BH mass function for the local Universe, using broad-line AGNs and virial BH mass estimates. By looking at very narrow ranges in redshift and AGN luminosity, we have detected a break at $M_{\rm BH} \approx 10^{6.5} - 10^7\ M_\odot$. We now investigate what fraction of BHs are active as a function of BH (spheroid) mass, by computing the inferred shape of the inactive BH mass function, using the formalism of Marconi et al. (2004; see also Yu & Tremaine 2002; Shankar et al. 2004; McLure & Dunlop 2004). Statistically speaking, the fraction of currently active systems may be interpreted as a duty cycle for BHs in that mass range.

Marconi et al. compute consistent inactive mass function from a variety of optical and near-infrared surveys and so for simplicity we use the Kochanek et al. (2001) *K*-band galaxy luminosity function. The galaxy luminosity and BH mass functions are linked through the *K*-band $M_{\rm BH} - L_{\rm bulge}$ relation of Marconi & Hunt (2003), assuming an intrinsic scatter in that relation of 0.3 dex and using Monte Carlo realizations to incorporate measurement uncertainties. The resulting uncertainties (see their Fig. 2*b*) are relatively constant for $M_{\rm BH} \lesssim 10^8\ M_\odot$, and have an amplitude of $\sigma \approx 0.2$ dex, although there are a variety of systematic uncertainties that preferentially impact the low-mass regime (for comparison, the Shankar et al. mass function is ~ 0.5 dex higher than Marconi et al. at $M_{\rm BH} = 10^7 M_\odot$). At high mass, the mass function is well-constrained; the luminosity of elliptical galaxies may be translated directly into BH mass. On the other hand, to properly translate between galaxy luminosity and BH mass at low luminosities requires knowledge of the (poorly constrained) luminosity function of bulges. For the moment, we simply adopt the fiducial values from Marconi et al., who assume morphological fractions ($m_{\rm bulge} - m_{\rm total}$) from Fukugita et al. (1998) of 11% elliptical, 21% S0, 43% Sab, and 19% Scd and bulge-to-disk values from Aller & Richstone (2002; derived from the data of Simien & de Vaucouleurs 1986) of 0.64 ± 0.30 for S0, 1.46 ± 0.56 for Sab, and 2.86 ± 0.59 for Scd galaxies. We show the resultant distribution of inactive BH mass as a dashed line in Figure 11*a*. For reference, the contribution from early- and late-type spirals within the adopted formalism are shown in long and short dot-dash lines, respectively.

The active fraction clearly depends strongly on BH mass. The differences in shape between active and inactive systems is highlighted in Figure 11*a*, where the active mass function is boosted by a factor of ~ 200 to overlay the inactive mass function derived as described above. (Because the low-mass slope is particularly uncertain, we also show the best-fit slope to the lowest-mass and redshift bin from §4.4 [*dotted*]). In the bottom panel we show the ratio of each subpopulation with the inactive mass function. BHs with masses $\sim 10^7\ M_\odot$, living in $\sim 10^{10}\ M_\odot$ spheroids are active $\sim 0.4\%$ of the time. At higher BH mass the number of active BHs drops quickly; local massive BHs are not radiating at substantial fractions of their Eddington limit. The same behavior was seen by Heckman et al. (2004) for narrow-line AGNs. It is reassuring that we find consistency with the results of Heckman et al., despite our differing (indirect) means of measuring $M_{\rm BH}$. The Heckman et al. result, and now ours, may be seen as confirmation of the suggestion, based on AGN luminosity functions, that lower-mass objects build their mass at low redshift, while the most massive BHs

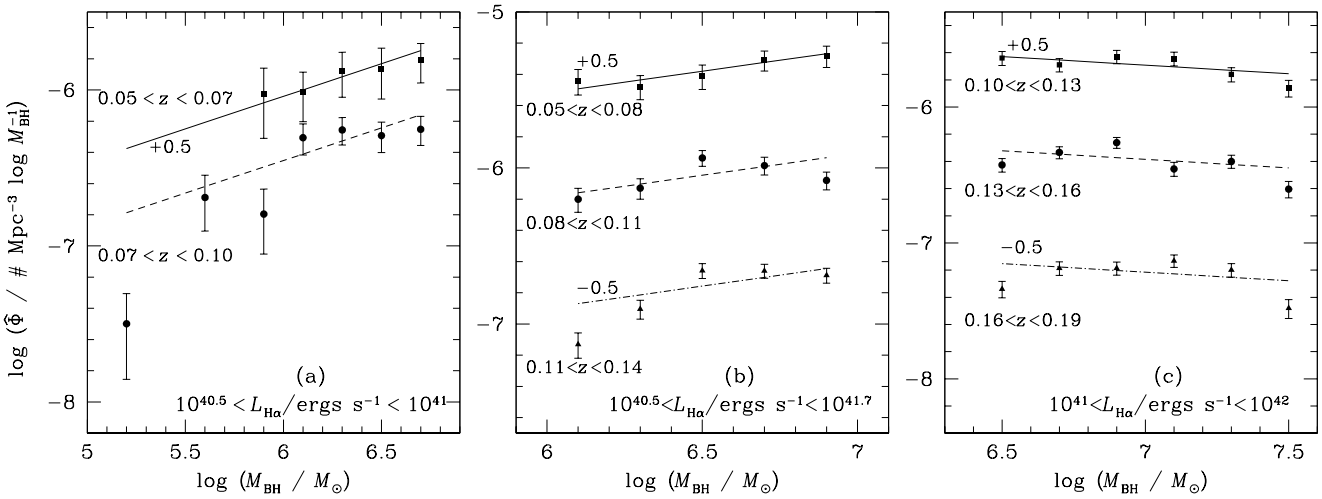

FIG. 9.— Fits to the BH mass function in narrow ranges of $M_{\rm BH}$, $L_{\rm H\alpha}$, and z, as indicated. These windows were selected to have uniform sensitivity to galaxy fiber luminosity, so that the measured slopes represent physical changes in space density. We perform simultaneous power-law fits (allowing different amplitudes but fixing the slopes between bins) to the redshift bins shown in each panel. We clearly detect a break in the mass function in the mass range $10^{6.5}-10^{7}\ M_{\odot}$, although the exact location is not clear from these data. Note also that we are only sensitive to active galaxies with a narrow range of fiber luminosities, which may bias these results (see text).

completed their growth at high redshift ("cosmic downsizing"; Cowie et al. 1996; Ueda et al. 2003; Steffen et al. 2003).

There is an important caveat that deserves discussion. While Marconi et al. (as well as Shankar et al. and McLure & Dunlop) find good agreement between inactive mass functions derived from galaxy luminosity and σ_* functions, Tundo et al. (2007) report that the mass function based on σ_* distributions is systematically lower than that based on galaxy luminosity functions.

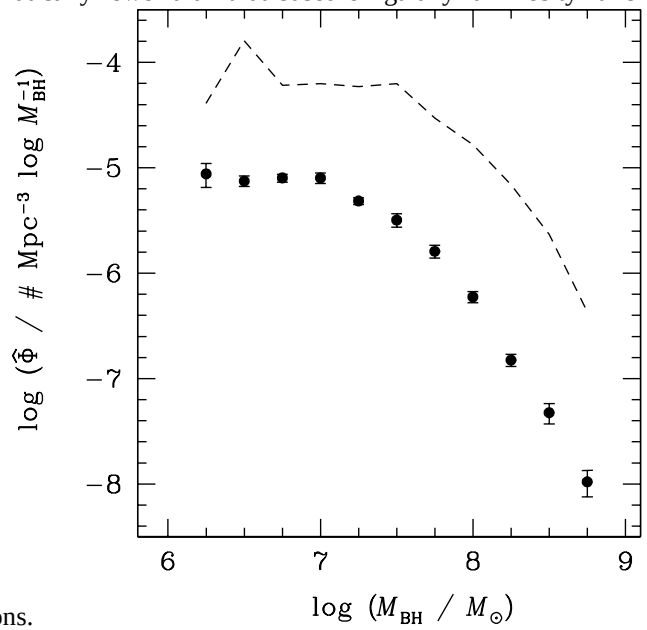

FIG. 10.— Comparison between the BH mass function of broad-line (*filled symbols*; this paper, truncated at $10^6\ M_{\odot}$ for consistency with the narrow-line AGN sample) and narrow-line (*dashed line*; Heckman et al. 2004) AGNs. Mass function for broad-line objects as described above. Volume corrections for the narrow-line objects are based solely on the galaxy color and luminosity. The space density of narrow-line objects in their sample is significantly higher than what is seen for broad-line objects, due to the relative ease of detecting high-EW narrow lines.

According to Bernardi et al. (2007), the $M_{\rm BH}-\sigma_*$ calibration sample (e.g., Tremaine et al. 2002) has a biased Faber-Jackson (1976) relation compared to the SDSS, in the sense that the galaxies have lower luminosities at a given σ_* (or higher σ_* at a given L). One consequently infers a lower BH mass function from the $M_{\rm BH}-\sigma_*$ relation than from the $M_{\rm BH}-L_{\rm bulge}$ relation. Bernardi et al. (2007) present a model in which the $M_{\rm BH}-\sigma_*$ relation provides the more reliable estimator of BH mass density. If (and this is by no means certain) they have properly modeled the bias, then the true inactive BH mass density should be ~ 0.5 dex lower at $M_{\rm BH}= 10^9\ M_{\odot}$, and the active fraction declines less steeply with mass than we report here. At the present time, given the systematic differences between authors and estimators, we conservatively assign a factor of 3 uncertainty to our active fraction across all mass bins.

It is also worth noting that the active fraction depends sensitively on the depth of the survey. The Palomar spectroscopic survey of galaxies, which is significantly more sensitive to low-luminosity Hα lines, finds an active fraction of ~ 60 % in nearby, bulge-dominated galaxies (Ho et al. 1997b). Despite the limited dynamic range in our sample, the number density of sources at a given BH mass increases at lower Eddington ratio, modulo incompleteness (Fig. 11*b*).

Aside from the known decrease of active fraction at high BH mass, we additionally see a decline in active fraction for BHs $\lesssim 10^{6.5}\ M_{\odot}$, but unlike the case of massive BHs, we cannot clearly interpret the decline. Taken at face value, the observation suggests that as we move to masses below the peak, the duty cycle declines. Unfortunately, both the active and inactive mass functions are highly uncertain for masses $< 10^{6.5}\ M_{\odot}$. Ultimately, we are limited by our knowledge of (a) the shape of the luminosity function, (b) the conversion between galaxy luminosity and BH mass for systems that contain BHs, and (c) the occupation fraction of BHs in dwarf galaxies. We discuss the potential magnitude and impact of each of these effects below.

First of all, the luminosity function of Kochanek et al. (2001) is measured only to a luminosity of $M_K = -20$ mag, or a BH mass of $10^{6.4}\ M_{\odot}$ for an elliptical galaxy, or $10^{5.1}\ M_{\odot}$ for an Scd galaxy. Thus, the entire low-mass regime involves some extrapolation. Deeper luminosity functions do exist (e.g., Blanton et al. 2005), but we are still left with the highly uncertain task of converting between an observed luminosity function and a BH mass function. The morphological fractions adopted by

Marconi et al. (2004; from Fukugita et al. 1998) are relatively well-determined for E/S0 galaxies. They are adopted from the morphology-density study of Postman & Geller (1984), based on the CfA redshift survey (Huchra et al. 1983; morphologies from de Vaucouleurs et al. 1976 and Nilson 1973), which separated galaxies into E, S0, and spiral using visual classification. On the other hand, the fractions of Sab and Scd galaxies are derived in a less-direct fashion. Tinsley (1980) took the observed color and apparent magnitude distributions from the photographic plate study of Kirshner et al. (1978) and solved simultaneously for the morphological fractions and redshifts that reproduced the observations, using broad-band color distributions from Pence (1976). Because of the degeneracies inherent in photometric redshifts based on two broad-band colors[4], and the limited sample size ($\sim$ 800 galaxies), this leads to significant uncertainties in the bulge fractions for spiral galaxies.

Ideally, we would like a direct measurement of bulge (rather than total galaxy) luminosity. Džanović et al. (2007; see also Tasca & White 2007) present spheroid luminosity and mass functions based on two-dimensional image decomposition of $\sim$ 9000 SDSS galaxies. The resulting BH mass function is consistent with a decrease in BH mass density of $\sim$ 0.5 dex between $M_{\rm BH} = 10^7\ M_\odot$ and $M_{\rm BH} = 10^5\ M_\odot$. However, the conversion from spheroid mass to BH mass relies on extrapolation of BH-bulge relations that have been calibrated only for higher masses. The host galaxies of low-mass BHs ($M_{\rm BH} < 10^6\ M_\odot$) may not even contain bulges. Indeed, neither of the two best-studied low-mass BHs ($M_{\rm BH} \approx 10^5\ M_\odot$)—NGC 4395 (Filippenko & Ho 2003) or POX 52 (Barth et al. 2004)—contains a classical bulge. The former is a late-type, bulgeless spiral, which lies on the low-mass extrapolation of the $M_{\rm BH} - L_{\rm bulge}$ relation only if one considers the luminosity of its nuclear star cluster. POX 52 is a dwarf spheroidal galaxy[5], and from the total luminosity of the host one would predict a BH mass 50 times higher than its virial mass or σ_* suggests. A similar trend is seen for the SDSS sample of Greene & Ho (2004; J. E. Greene et al., in preparation). It is possible that these more distant systems also obey an $M_{\rm BH} - L_{\rm bulge}$ relation with a nuclear star cluster, and POX 52 may show evidence of nucleation from *HST* observations (C. J. Thornton et al., in preparation), but in general it is not possible to predict nuclear cluster luminosity from galaxy luminosity (although the two may be correlated; Ferrarese et al. 2006; Rossa et al. 2006; Wehner & Harris 2006). In short, a conversion from galaxy luminosity to BH mass is presently unconstrained for BHs with masses $M_{\rm BH} < 10^6\ M_\odot$.

Finally, while we believe that most (if not all) bulges host BHs, the occupation fraction of BHs in late-type galaxies in unknown. Dynamical measurements in the Local Group for the late-type galaxy M33 (Gebhardt et al. 2001) and the dwarf spheroidal galaxy NGC 205 (Valluri et al. 2005) show that neither hosts a BH with a mass in accordance with expectations from the $M_{\rm BH} - \sigma_*$ relation. On the other hand, the massive globular cluster G1 in Andromeda hosts a BH in accord with the $M_{\rm BH} - \sigma_*$ relation (Gebhardt et al. 2002, 2005), and NGC 4395, POX 52, and the Greene & Ho (2004) sample, all late-type galaxies hosting BHs with masses $< 10^6\ M_\odot$, are consistent with the low-mass extrapolation of the $M_{\rm BH} - \sigma_*$ relation (Filippenko & Ho 2003; Barth et al. 2004, 2005).

In light of these many uncertainties, it is difficult to interpret the apparent decrease in active fraction at low mass. The most straightforward interpretation may be that the shape of the active mass function actually traces the shape of the bulge luminosity function at low luminosity. Otherwise, is it is difficult to understand why late-type spiral galaxies, with a ready gas supply, nevertheless are preferentially inactive. The distribution of activity in the Palomar spectroscopic survey of nearby galaxies support this hypothesis; Ho et al. (1997b) find that Seyfert galaxies (i.e., objects with relatively high accretion rates) are predominantly found in early-type spiral galaxies (Sa–Sb). In the future, with the availability of more complete measurements of spheroid luminosity functions, we may use our observations of active fractions to measure the mass at which the BH occupation fraction departs from unity.

5.2. *Connection to Higher Redshift*

Broad-line AGN activity at the present day is dominated by $\sim 10^7\ M_\odot$ BHs radiating at $\sim$ 10% of their Eddington limits (Fig. 11*b*). During the quasar epoch, $1 < z < 3$, BH mass growth is dominated by optically bright, near-Eddington growth of massive BHs (e.g., Vestergaard 2002) and this growth basically accounts for most of the total BH mass density observed today (e.g., Yu & Tremaine 2002). Even as one moves to lower luminosities, BH growth appears to be dominated by near-Eddington accretion, at least for massive BHs at high redshift (Kollmeier et al. 2006). In general, this picture sits comfortably with the observation that massive elliptical galaxies (hosts of the most massive BHs) formed their stars rapidly at high redshifts (e.g., Bower et al. 1992; Trager et al. 2000; Thomas et al. 2005). It is the redshift range between the present and $z \approx 1$ that remains poorly constrained. From the point of view of galaxy evolution, there appears to be a significant (factor of 2) increase in the mass density of spheroids over this interval (e.g., Brown et al. 2007; Faber et al. 2007). It would be interesting to know whether any commensurate BH growth occurred.

There are tantalizing hints. Optical QSO luminosity functions show that massive BHs are not radiating at high Eddington ratio below $z \approx 1$ (e.g., Richards et al. 2006), but do not constrain the evolution of low-luminosity sources. X-ray luminosity functions, built from very deep *Chandra* and *XMM-Newton* pointings, are able to probe significantly fainter luminosities (see Brandt & Hasinger 2005 for a recent review). It is clear that the space density of low-luminosity ($L_{\rm X} \approx 10^{42} - 10^{43}$ ergs s^{-1}), X-ray–selected sources peaks at considerably lower redshift ($z \approx 0.7$) than higher-luminosity sources. Unfortunately, multiple scenarios for BH growth result in similar luminosity evolution. At one extreme, one may imagine all near-Eddington growth at all masses occurs at high redshift and then slowly shuts off, while at the other extreme, one may imagine that the low-luminosity radiation is dominated by the growth of low-mass BHs, which acquire a significant fraction of their mass at low redshift. In reality, some combination of these two scenarios presumably occurs. The latter hypothesis, dubbed "cosmic downsizing," is often preferred in the literature, partially because galaxies display similar behavior (e.g., Cowie et al. 1996; Barger et al. 2005).

[4]For instance, Fukugita et al. (1995) find that the *K*-corrections for Sa–Sc galaxies at $z \lesssim 0.3$ differ by $\delta z \lesssim 0.1$, in *B* or *V*. Degeneracies between metallicity and age only add to the uncertainties.

[5]Such objects are commonly referred to as dwarf elliptical galaxies in the literature. However, because their structure is quite different from that of classical elliptical galaxies, we prefer to refer to them as dwarf spheroidal systems.

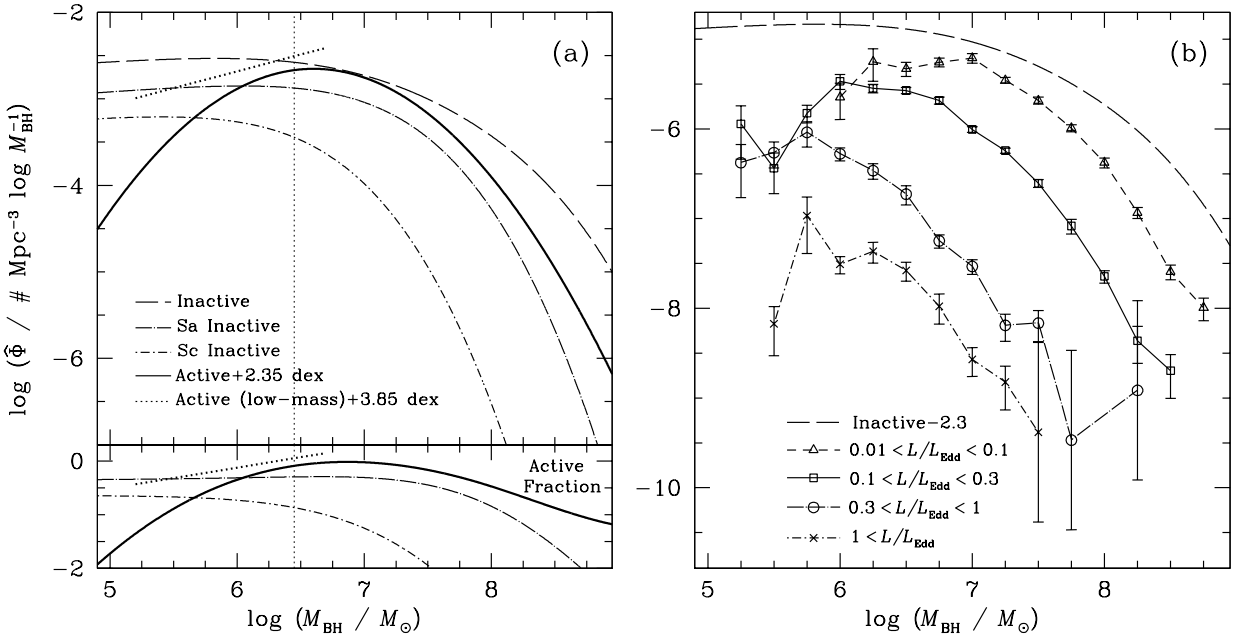

FIG. 11.— (*a*) Comparison of the inactive BH mass function with the broad-line BH mass function. The inactive mass function is derived from the galaxy luminosity function of Kochanek et al. (2001), using the formalism of Marconi et al. (2004), including an intrinsic dispersion of 0.3 dex in the relation between galaxy luminosity and BH mass. We show the log-normal fit to the active BH mass function offset by 2.35 dex (*solid*) and the best-fit power law to the lowest-mass, lowest-z bin (Fig. 9*a*) to demonstrate the uncertainty in slope and break position at the low-mass end. The ratio between the total inactive mass function and each population is shown in the bottom panel. The vertical line indicates the point at which we begin to use an extrapolation of the luminosity function. (*b*) Comparison of the inactive BH mass function (*dashed*) with the active mass function in different Eddington ratio bins (*solid symbols*). Bins with > 3 points are shown. It is clear that all high-mass BHs are radiating at very low Eddington ratios.

The first concrete evidence in support of downsizing came from the Heckman et al. (2004) study, which showed unambiguously that local accreting BHs are typically an order of magnitude less massive than the typical local inactive BH. The present study finds the same result. However, we still must ask whether X-ray–selected AGNs at $z = 0.7$ are really the same population as local optically selected sources. The story may not be so straightforward. Netzer & Trakhtenbrot (2007) find that the typical BH mass and Eddington ratio of optically selected AGNs both increase significantly from the present time to $z = 0.7$, so that what we measure locally may no longer apply at that epoch. The other intriguing, but not definitive, evidence comes from recent optical studies of the host galaxies of X-ray–selected AGNs. It seems that the majority of sources are found in massive, relatively red galaxies (e.g., Colbert et al. 2005; Nandra et al. 2007; see also Barger et al. 2005). The clustering properties of X-ray–selected AGNs also suggest that the hosts are typically more massive than optically-selected AGNs at the same redshift (e.g., Coil et al. 2007, Miyaji et al. 2007, Coil, A. L. private communication). Assuming that the $M_{\rm BH} - \sigma_*$ relation is largely in place at $z \approx 0.7$ (Peng et al. 2006; Salviander et al. 2007; but see also Treu et al. 2004; Woo et al. 2006), the observed galaxy luminosities correspond to BHs with masses $> 10^8\ M_\odot$, casting doubt on the cosmic downsizing scenario for this population.

Taken at face value, the fact that X-ray–selected samples are found in very luminous host galaxies suggests that low-luminosity, hard X-ray–selected sources consist predominantly of massive BHs in a low-Eddington state. These sources are known to be an intrinsically hard population with no big blue bump (Ho 1999), and if they have broad lines, they will be extremely low contrast, and thus difficult to detect. The conjecture that low-Eddington sources dominate the hard X-ray population thus accounts for both the general lack of apparent broad emission and the generic hard spectral shape of the X-ray background (see additional arguments in Shen et al. 2007). On the other hand, low-luminosity, soft X-ray–selected sources, most likely closely linked to optically selected broad-line AGNs, also have a peak space density at low redshift (e.g., Hasinger et al. 2005). At the present time, it is unclear whether the massive host galaxies measured in the studies above are representative of the population as a whole. An unbiased comparison of the Eddington ratio distributions of the soft and hard X-ray–selected samples is needed.

A rather different approach to constraining the evolution of BH mass density is taken by Merloni (2004). He constructs a BH mass function using constraints from the joint X-ray and radio luminosity function, in combination with an empirical relation between BH mass and X-ray and radio luminosity (the "fundamental plane"; e.g., Merloni et al. 2003). He finds fast evolution; by $z = 0.6$ the characteristic accreting BH mass has increased from $10^7\ M_\odot$ to $10^8\ M_\odot$. However, his analysis also tends to favor low-Eddington sources, and indeed his characteristic $L_{\rm X}/L_{\rm Edd}$ never exceeds 1%. Ideally, work like that presented here may be extended to higher redshift to directly address the distribution of BH mass at intermediate redshift.

6. SUMMARY

We present the first measurement of the local BH mass function for broad-line active galaxies. Our sample of ~ 9000 galaxies is drawn from the Fourth Data Release of the Sloan Digital Sky Survey, based on the presence of broad Hα emission. Our Hα luminosity function is found to be consistent with previous measurements, and with the local soft X-ray luminosity function. Using standard scaling relations between AGN luminosity and line width, we derive BH masses for the entire sample. Much like the Heckman et al. (2004) sample of narrow-line AGNs, the typical BH in our sample has a mass of $M_{\rm BH}$

$\approx 10^7\ M_\odot$ and an Eddington ratio of $L_{\rm bol}/L_{\rm Edd} \approx 10\%$. Although we are highly incomplete for low-Eddington ratio systems, by looking at very narrow bins in $M_{\rm BH}$, $L_{\rm H\alpha}$, and z we find clear evidence for a true turnover in space density below $M_{\rm BH} \approx 10^{6.5} - 10^7\ M_\odot$. Compared to the inferred shape of the mass function of inactive BHs, the mass function of active BHs falls significantly both above and below this characteristic break mass. The dearth of active massive BHs is a familiar result—massive BHs are mostly quiescent in the local Universe. The decreasing space density at low BH mass presumably reflects the fact that bulge fraction and BH occupation fraction both decrease in dwarf galaxies.

One of the major motivations of this study was to constrain the shape of the BH mass function for BHs with masses $< 10^6\ M_\odot$, since broad-line AGN surveys currently have the unique capability to explore this mass regime. We have found evidence for a decreasing space density of active BHs with masses $< 10^{6.5}\ M_\odot$, at least for objects with host galaxies more luminous than $M_B \approx -16$ mag. However, substantial work remains to determine the true demographics of BHs in low-mass galaxies. Measurements that isolate the luminosity and mass functions of spheroids (e.g., Džanović et al. 2007) on the one hand, combined with empirical conversions between spheroid luminosity and BH mass in the low-mass regime (J. E. Greene et al., in preparation) on the other, will provide predictions for the shape of the inactive BH mass function for $M_{\rm BH} < 10^6\ M_\odot$. At the same time, alternate search techniques, which are less sensitive to host galaxy luminosity, are required to discover low-mass, low $L_{\rm bol}/L_{\rm Edd}$ BHs. Apart from deeper nuclear optical spectroscopic surveys, deep X-ray and radio surveys may provide sensitivity to lower-Eddington ratio systems and eliminate the host luminosity bias suffered by the present study. Finally, future time-domain surveys may place limits on the frequency of flares from the tidal disruption of stars captured by BHs in dwarf galaxies (e.g., Rees 1988; Donley et al. 2002; Gezari et al. 2006; Milosavljević et al. 2006).

We gratefully acknowledge useful conversations with M. Bernardi, L. Hao, J. P. Ostriker, J. A. Kollmeier, and, particularly, M. A. Strauss. We appreciate a timely report from the anonymous referee. Finally, we thank the entire SDSS team for providing the fantastic data products that made this work possible. Support for J. E. G. was provided by NASA through Hubble Fellowship grant HF-01196 awarded by the Space Telescope Science Institute, which is operated by the Association of Universities for Research in Astronomy, Inc., for NASA, under contract NAS 5-26555. L. C. H. acknowledges support by the Carnegie Institution of Washington and by NASA grant SAO 06700600. Funding for the SDSS has been provided by the Alfred P. Sloan Foundation, the Participating Institutions, the National Science Foundation, the U.S. Department of Energy, the National Aeronautics and Space Administration, the Japanese Monbukagakusho, the Max Planck Society, and the Higher Education Funding Council for England. The SDSS web site is `http://www.sdss.org/`.

APPENDIX

A. MEASUREMENT UNCERTAINTIES

We describe a suite of simulated galaxy spectra that we have built to investigate the reliability of our BH mass measurements over the Hα luminosity range of interest, for SDSS-quality data. We investigate our ability to recover the input FWHM$_{\rm H\alpha}$, $L_{\rm H\alpha}$, and $M_{\rm BH}$ as the Hα flux, galaxy continuum, and S/N of the spectra change. We also justify our particular choice of detection thresholds in rms-normalized flux and EW(Hα). At the same time, we investigate the importance of factors such as strength of the narrow lines, shape of the stellar continuum, and the slope of the AGN continuum. The basic grid of simulations spans a range of $10^4 < M_{\rm BH}/M_\odot < 10^9$, $0.01 < L_{\rm bol}/L_{\rm Edd} < 3$, and $5 <$ S/N < 50. As we have noted previously, the level of galaxy continuum may play a crucial role in our ability to measure the broad Hα component at all. We have decided to assign the galaxy luminosity based roughly on scaling relations between the BH and the surrounding galaxy. While there is large scatter in such scaling relations, we attempt to span a reasonable range of galaxy luminosities, so that at least we are simulating realistic conditions.

All of the spectral properties are derived from the chosen $M_{\rm BH}$, $L_{\rm bol}/L_{\rm Edd}$, and S/N. In terms of the AGN features, the continuum luminosity and FWHM$_{\rm H\alpha}$ are determined using the formulae presented in Greene & Ho (2005b). A small fraction (10%) of the total broad emission luminosity is placed in a very broad component, since such broad wings are often seen in actual spectra. The AGN continuum shape is given slopes of $\beta = 1.5, 1.0$, and 0.5, where $f_\beta \propto \lambda^{-\beta}$. Using the Tremaine et al. (2002) $M_{\rm BH} - \sigma_*$ relation, we calculate the width of the narrow-line region components, assuming that the velocity dispersion of the narrow lines is equal to that of the bulge (e.g., Nelson & Whittle 1996; Greene & Ho 2005a), while the narrow-line flux is fixed using the empirical relation of Zakamska et al. (2003), which relates $L_{\rm [OIII]}$ to L_{5100}. Finally, all lines are convolved to the typical velocity resolution of the SDSS, $\sigma \approx 71$ km s^{-1} (e.g., Heckman et al. 2004).

In terms of the host galaxy, we again assume the $M_{\rm BH} - \sigma_*$ relation holds, and associate a stellar velocity dispersion and bulge luminosity with each BH. For elliptical galaxies, this is the entire story, but at low $M_{\rm BH}$, the hosts are typically spiral galaxies. Therefore, we need a way to estimate the total galaxy luminosity based on the bulge properties. The $M_{\rm BH} - \sigma_*$ relation of Tremaine et al. (2002) links each input BH with a σ_*. Then, using the relation between σ_* and maximum circular velocity $v_{\rm c}$ (e.g., Ferrarese 2002; Baes et al. 2003; Pizzella et al. 2005) to obtain $v_{\rm c}$, the Tully-Fisher relation (Tully & Fisher 1977) may be used to estimate a total galaxy luminosity for a spiral host. In particular, we use the best-fit Tully-Fisher relation from Masters et al. (2006) for their "in+" sample, and we neglect variations in the relation with Hubble type. We incorporate the scatter in both the $v_{\rm c}$-σ_* relation and the Tully-Fisher relation by perturbing each fit parameter by a log-normally distributed deviate drawn from the best-fit distribution. For a given BH, we must decide whether to place it in a spiral or elliptical host galaxy. There is, of course, a limit to how bright a spiral galaxy may be and, conversely, to the faintest elliptical galaxies. For the latter, we adopt the luminosity of M32 ($M_B = -15.8$ mag; Tremaine et al. 2002), while for the former we adopt a limit of $M_I > -24$ mag, which represents the brightest galaxies in the Masters et al. sample. We note that M32 is fainter than POX 52, which is a dwarf spheroidal galaxy known to host a BH of mass

$\sim 10^5\ M_\odot$ (Barth et al. 2004). This is because dwarf spheroidal galaxies are more luminous than elliptical galaxies at the same σ_* (e.g., Geha et al. 2003). If the calculated bulge luminosity is too faint, the object is assigned only a spiral host, and conversely if the luminosity is bright enough, the object is assigned an elliptical host. BHs in the mass range of $10^{6.5}-10^8\ M_\odot$ are typically assigned both, which is in good agreement with observations. The stellar continuum shape is provided by the eigenspectra presented in Yip et al. (2004). For the majority of the simulations, we use a pure absorption-line spectrum typical of an elliptical galaxy, by combining their first three eigenspectra with weights [1,1,0.9]. We have investigated the impact of younger stellar populations, using weights [0.1,0.0,–0.5] to represent a typical Sc galaxy, and [0.0,0.0,–0.5] to represent a post-starburst system. We

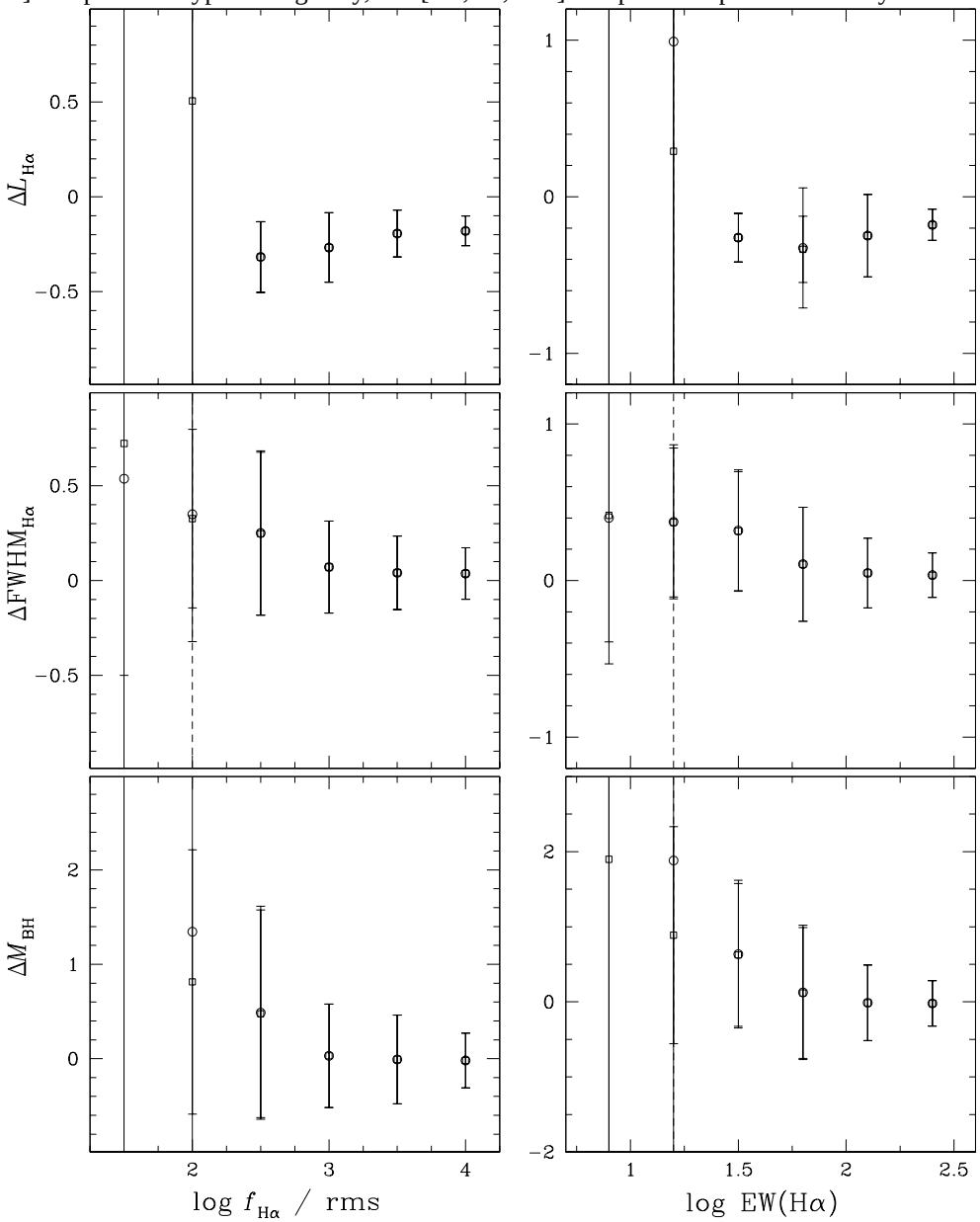

FIG. A12.— Deviation Δ = (out–in)/in, from the measured properties $L_{\rm H\alpha}$, FWHM$_{\rm H\alpha}$, and the inferred $M_{\rm BH}$ for all simulations. We show the deviations in (*left*) logarithmic bins of Hα flux normalized by the local rms and (*right*) EW(Hα). The entire sample in each bin is shown as an open circle, while the sub-sample with the joint flux and EW cuts are shown as open squares; they only differ at and below the detection thresholds. Objects that have been rejected by our initial detection are not included, but those below our detection threshold are, so that we may justify our choices. The detection thresholds are indicated by dotted lines.

find that changes in stellar populations do not significantly impact our derived masses; the PCA method of Hao et al. (2005a) is quite robust for our purposes.

Each artificial spectrum is run through our entire detection algorithm. Continuum subtraction is performed using PCA, the Hα detection is performed, and then the line fitting is performed to see if the broad lines are detectable at this S/N. Objects that would be rejected by our initial Hα detection algorithm are not included in the investigation of parameters shown below, but we do not remove objects below our detection threshold, since it is our goal to demonstrate that we have chosen reasonable values. We quantify the dependence of the measurements on normalized flux and EW(Hα) by plotting as a figure of merit the fractional deviation $\Delta X \equiv (X_{\rm out}-X_{\rm in})/X_{\rm in}$. Specifically, we calculate $\Delta L_{\rm H\alpha}$, $\Delta{\rm FWHM}_{\rm H\alpha}$, and $\Delta M_{\rm BH}$. Note that these deviations are plotted in linear (not logarithmic) space. A factor of 2 error in $M_{\rm BH}$ corresponds to $\Delta M_{\rm BH}$=1. We show in Figure A12 the dependence of ΔX on

the rms-normalized flux and EW(Hα) for each parameter. The detection threshold is noted as a dotted line in each panel. It is quite clear from these figures that below our chosen detection thresholds we incur completely unacceptable uncertainties in the derived parameters. We have run smaller sets of simulations to test the importance of both the narrow-line region strength and the underlying galaxy continuum shape, and we find that the deviations in $L_{\rm H\alpha}$, FWHM$_{\rm H\alpha}$, and $M_{\rm BH}$ are constant as a function of these parameters. If anything, low-mass BHs are slightly more likely to be included in our sample when the narrow-line strength is high compared to our fiducial choice.

B. MAXIMUM LIKELIHOOD

While the $V/V_{\rm max}$ method used in §4.1 is extremely intuitive, the resulting luminosity functions may be biased due to local inhomogeneities in the distribution of galaxies, as well as peculiar motions within the Local Supercluster (e.g., Efstathiou et al. 1988). In the maximum likelihood method, rather than parameterizing the AGN selection function as a maximum observable volume, each source is assigned a probability of detection as a function of Hα luminosity, $p_i(L_{\rm H\alpha})$. Then, the likelihood that we observe our particular sample may be expressed as

$$\mathcal{L} = \frac{\prod_i p_i(L_i)\Phi(L_i)dL_i}{\int p_i(L_i)\Phi(L)dL}. \tag{B1}$$

Our goal is to maximize this function, or equivalently minimize $S \equiv -2\ln\mathcal{L}$. Rather than assume a particular form for the underlying luminosity function, we derive a stepwise-constant, non-parametric function. In detail, we follow the iterative procedure outlined in Blanton (2000; see also Koranyi & Strauss 1997; Hao et al. 2005b).

The primary challenge is in deriving the selection function, or the probability of observing a given object as a function of luminosity. We attempt to follow closely the technique of Hao et al. (2005b) for ease of direct comparison. Given the flux limits of the SDSS, each source has both a minimum and a maximum luminosity at which we may observe it. As $L_{\rm H\alpha}$ increases, we increase the power-law luminosity of the AGN according to the relation of Greene & Ho (2005b), and the maximum luminosity is reached when the source reaches either its Eddington luminosity, or the bright limit of the SDSS. The minimum luminosity is more complicated to calculate. It is reached either when the source reaches a magnitude limit, or when the Hα line is no longer detectable using our algorithms. For objects targeted as galaxies, this is relatively straightforward to determine. At each luminosity, we calculate the new total magnitudes and corresponding typical S/N. The minimum luminosity is reached when the source reaches our detection threshold ($f_{\rm H\alpha}/{\rm rms} < 200$) or the galaxy magnitude limit. For the objects targeted as QSOs, the situation is somewhat complicated by the possibility that the object changes target selection from QSO to galaxy as the source fades. The AGN contribution is estimated from the Hα luminosity. We adopt a very ad hoc prescription, in which the object is converted from a QSO to a galaxy when the AGN accounts for less than 10% of the total Petrosian magnitude. In practice, the number we choose does not affect our results, since in the vast majority of cases the limit is set by the detection threshold.

Within the limiting magnitudes, the AGN will have different detection thresholds depending on the contrast of the Hα luminosity and the S/N. As the Hα luminosity decreases for a given source, several important properties of the spectrum will change. The continuum level will decrease, of course, but since the BH mass is not changing, the line shape also must change. Progressively, as objects move to lower Eddington ratio, they grow more difficult to find, as their Hα flux is distributed more and more broadly, and the overall S/N of the spectrum decreases in parallel. In terms of detection efficiency, as we show in Appendix A, the galaxy type and luminosity only provide secondary corrections to our detection efficiency, which depends most strongly on line luminosity, line strength, and S/N. For that reason, we use our suite of simulated AGNs that span a wide range in $M_{\rm BH}$, $L_{\rm bol}/L_{\rm Edd}$, and S/N, as described in above. Our procedure is the following. We step between the minimum and maximum luminosity in steps of 0.5 dex (a factor of 3 in luminosity), and recalculate the total magnitude and thus typical S/N of the source. Using the measured $M_{\rm BH}$ and the new $L_{\rm H\alpha}$, we also assign an Eddington ratio to each source. All simulations with similar $M_{\rm BH}$, $L_{\rm bol}/L_{\rm Edd}$, and S/N are then selected, and a weighted-mean detection fraction is calculated (that is, we assign more weight to the objects with the most comparable values in each parameter). The benefit of this approach is that the mass-dependent biases highlighted above are built into the calculation. We are assuming, however, that the galaxy level scales with the BH mass. If this assumption is severely violated, then the galaxy light may overwhelm the AGN light more rapidly than assumed in these simulations.

Using the calculated minimum and maximum luminosities and detection fractions, we derive the maximum likelihood luminosity function shown in Figure 5. That we find such good agreement using two different methodologies is very encouraging. As an additional test, we divide our sample into redshift bins and verify that our maximum likelihood luminosity function, combined with the detection fractions calculated above, accurately predicts the observed distribution of $L_{\rm H\alpha}$ in each bin (Sandage et al. 1979). Following Hao et al., we calculate, in each redshift bin, the predicted number of sources per $L_{\rm H\alpha}$ bin ($F_{\rm p}$) as:

$$F_{\rm p}(L)\Delta L = \sum_i \frac{p_i(L)\Phi(L)\Delta L}{\int p_i(L')\Phi(L')dL'}. \tag{B2}$$

We then compare the calculated $F_{\rm p}$ with the observed $L_{\rm H\alpha}$ distribution, as shown in Figure B13. As can be seen, the agreement is very satisfactory, suggesting that our luminosity function provides a good description of the data.

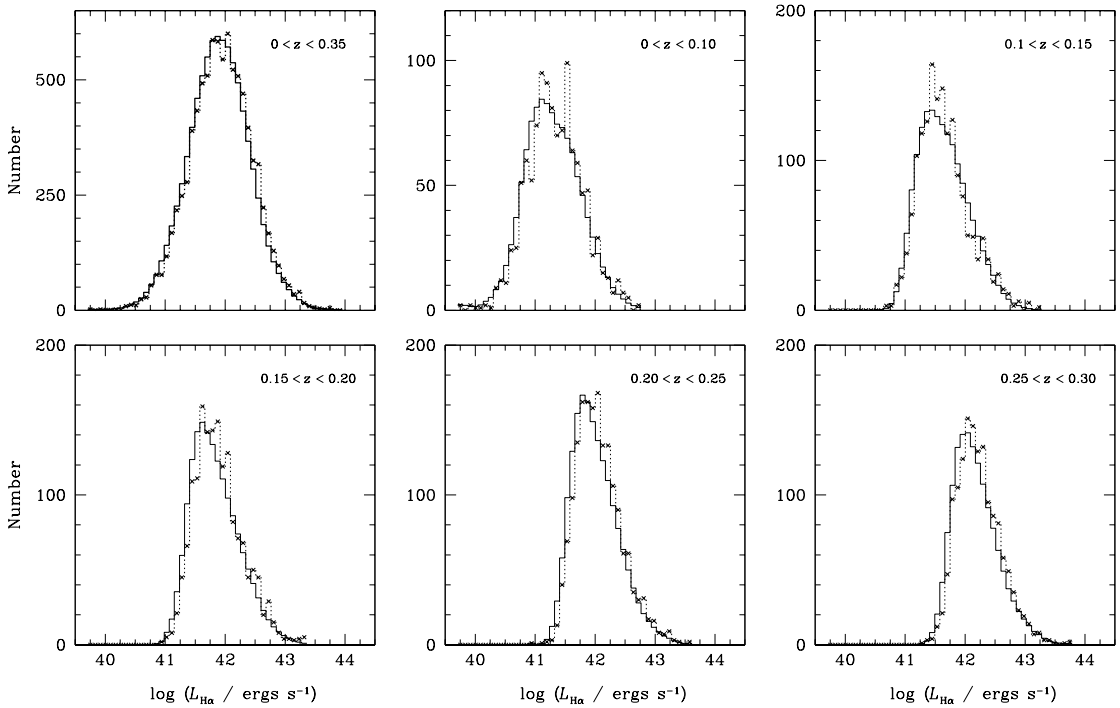

FIG. B13.— A comparison between the actual distribution of $L_{\rm H\alpha}$ (crosses and dotted lines) and that predicted by the luminosity function and detection fractions (solid histograms). Each panel shows a different redshift bin. The good agreement provides an important sanity check on our luminosity function.

REFERENCES

Adelman-McCarthy, J. K., et al. 2006, ApJS, 162, 38
Aller, M. C., & Richstone, D. 2002, AJ, 124, 3035
Baes, M., Buyle, P., Hau, G. K. T., & Dejonghe, H. 2003, MNRAS, 341, L44
Baldwin, J. A., Phillips, M. M., & Terlevich, R. 1981, PASP, 93, 5
Barger, A. J., Cowie, L. L., Mushotzky, R. F., Yang, Y., Wang, W.-H., Steffen, A. T., & Capak, P. 2005, AJ, 129, 578
Barth, A. J., Greene, J. E., & Ho, L. C. 2005, ApJ, 619, L151
Barth, A. J., Ho, L. C., Rutledge, R. E., & Sargent, W. L. W. 2004, ApJ, 607, 90
Becker, R. H., White, R. L., & Helfand, D. J. 1995, ApJ, 450, 559
Bentz, M. C., Peterson, B. M., Pogge, R. W., Vestergaard, M., & Onken, C. A. 2006, ApJ, 644, 133
Bernardi, M., et al. 2003, AJ, 125, 1817
Bernardi, M., Sheth, R. K., Tundo, E., & Hyde, J. B. 2007, ApJ, in press (astroph/0609300)
Blanton, M. 2000, ApJ, 544, 63
Blanton, M. R., Lupton, R. H., Schlegel, D. J., Strauss, M. A., Brinkmann, J., Fukugita, M., & Loveday, J. 2005, ApJ, 631, 208
Boroson, T. A., & Green, R. F. 1992, ApJS, 80, 109
Bower, R. G., Lucey, J. R., & Ellis, R. S. 1992, MNRAS, 254, 601
Brandt, W. N., & Hasinger, G. 2005, ARA&A, 43, 827
Brown, M. J. I., Dey, A., Jannuzi, B. T., Brand, K., Benson, A. J., Brodwin, M., Croton, D. J., & Eisenhardt, P. R. 2007, ApJ, 654, 858
Coil, A. L., Hennawi, J. F., Newman, J. A., Cooper, M. C., & Davis, M. 2007, ApJ, 654, 115
Colbert, J. W., Teplitz, H. I., Yan, L., Malkan, M. A., & McCarthy, P. J. 2005, ApJ, 621, 587
Collin, S., Kawaguchi, T., Peterson, B. M., & Vestergaard, M. 2006, A&A, 456, 75
Condon, J. J. 1989, ApJ, 338, 13
Cowie, L. L., Songaila, A., Hu, E. M., & Cohen, J. G. 1996, AJ, 112, 839
Croom, S. M., Smith, R. J., Boyle, B. J., Shanks, T., Miller, L., Outram, P. J., & Loaring, N. S. 2004, MNRAS, 349, 1397
de Vaucouleurs, G., de Vaucouleurs, A., & Corwin, H. G. 1976, University of Texas Monographs in Astronomy (Austin: Univ. Texas Press)
Donley, J. L., Brandt, W. N., Eracleous, M., & Boller, T. 2002, AJ, 124, 1308
Džanović, D., Benson, A. J., Frenk, C. S., & Sharples, R. 2007, MNRAS, submitted (astro-ph/0612719)
Efstathiou, G., Ellis, R. S., & Peterson, B. A. 1988, MNRAS, 232, 431
Faber, S. M., et al. 2007, ApJ, submitted (astro-ph/0506044)
Faber, S. M., & Jackson, R. E. 1976, ApJ, 204, 668
Favata, M., Hughes, S. A., & Holz, D. E. 2004, ApJ, 607, L5
Ferrarese, L. 2002, ApJ, 578, 90
Ferrarese, L., et al. 2006, ApJ, 644, L21
Ferrarese, L., & Merritt, D. 2000, ApJ, 539, L9
Ferrarese, L., Pogge, R. W., Peterson, B. M., Merritt, D., Wandel, A.,& Joseph, C. L. 2001, ApJ, 555, L79
Filippenko, A. V., & Ho, L. C. 2003, ApJ, 588, L13
Filippenko, A. V., & Sargent, W. L. W. 1988, ApJ, 324, 134
Fukugita, M., Hogan, C. J., & Peebles, P. J. E. 1998, ApJ, 503, 518
Fukugita, M., Shimasaku, K., & Ichikawa, T. 1995, PASP, 107, 945
Gebhardt, K., et al. 2000a, ApJ, 539, L13
——. 2000b, ApJ, 543, L5
——. 2001, AJ, 122, 2469
Gebhardt, K., Rich, R. M., & Ho, L. C. 2002, ApJ, 578, L41
——. 2005, ApJ, 634, 1093
Geha, M., Guhathakurta, P., & van der Marel, R. P. 2003, AJ, 126, 1794
Gezari, S., et al. 2006, ApJ, 653, L25
Greene, J. E., & Ho, L. C. 2004, ApJ, 610, 722
——. 2005a, ApJ, 627, 721
——. 2005b, ApJ, 630, 122
——. 2006a, ApJ, 641, 114
——. 2006b, ApJ, 641, L21
——. 2007, ApJ, 656, 84
Groves, B. A., Heckman, T. M., & Kauffmann, G. 2006, MNRAS, 371, 1559
Hao, L., et al. 2005a, AJ, 129, 1783
——. 2005b, AJ, 129, 1795
Hasinger, G., Miyaji, T., & Schmidt, M. 2005, A&A, 441, 417
Heckman, T. M., Kauffmann, G., Brinchmann, J., Charlot, S., Tremonti, C., & White, S. D. M. 2004, ApJ, 613, 109
Ho, L. C. 1999, ApJ, 516, 672
——. 2004, in Carnegie Observatories Astrophysics Series, Vol. 1: Coevolution of Black Holes and Galaxies, ed. L. C. Ho (Cambridge: Cambridge Univ. Press), 292
Ho, L. C., Filippenko, A. V., & Sargent, W. L. W. 1997a, ApJS, 112, 315
——. 1997b, ApJ, 487, 568
Ho, L. C., Filippenko, A. V., Sargent, W. L. W., & Peng, C. Y. 1997c, ApJS, 112, 391
Huchra, J. P., Davis, M., Latham, D., & Tonry, J. 1983, ApJS, 52, 89
Huchra, J. P., & Sargent, W. L. W. 1973, ApJ, 186, 433
Kaspi, S., Maoz, D., Netzer, H., Peterson, B. M., Vestergaard, M., & Jannuzi, B. T. 2005, ApJ, 629, 61
Kauffmann, G., et al. 2003, MNRAS, 346, 1055
Kirshner, R. P., Oemler, A., Jr., & Schechter, P. L. 1978, AJ, 83, 1549
Kochanek, C. S., et al. 2001, ApJ, 560, 566
Kollmeier, J. A., et al. 2006, ApJ, 648, 128
Koranyi, D. M., & Strauss, M. A. 1997, ApJ, 477, 36

Kraemer, S. B., Ho, L. C., Crenshaw, D. M., Shields, J. C., & Filippenko, A. V. 1999, ApJ, 520, 564
Krolik, J. H. 2001, ApJ, 551, 72
Marconi, A., & Hunt, L. K. 2003, ApJ, 589, L21
Marconi, A., Risaliti, G., Gilli, R., Hunt, L. K., Maiolino, R., & Salvati, M. 2004, MNRAS, 351, 169
Masters, K. L., Springob, C. M., Haynes, M. P., & Giovanelli, R. 2006, ApJ, 653, 861
McLure, R. J., & Dunlop, J. S. 2004, MNRAS, 352, 1390
Merloni, A. 2004, MNRAS, 353, 1035
Merloni, A., Heinz, S., & Di Matteo, T. 2003, MNRAS, 345, 1057
Merritt, D., Milosavljević, M., Favata, M., Hughes, S. A., & Holz, D. E. 2004, ApJ, 607, L9
Milosavljević, M., Merritt, D., & Ho, L. C. 2006, ApJ, 652, 120
Miyaji, T., et al. 2007, ApJS, accepted (astro-ph/0612369)
Nandra, K., et al. 2007, ApJ, 660, L11
Narayan, R. 2006, in From X-Ray Binaries to Quasars: Black Hole Accretion on All Mass Scales, ed. T. J. Maccarone, R. P. Fender, & L. C. Ho (Dordrecht: Kluwer), 177
Nelson, C. H., Green, R. F., Bower, G., Gebhardt, K., & Weistrop, D. 2004, ApJ, 615, 652
Nelson, C. H., & Whittle, M. 1996, ApJ, 465, 96
Netzer, H. 1990, in Active Galactic Nuclei, ed. R. D. Blandford, H. Netzer, L. Woltjer, T. Courvoisier, & M. Mayor, (Berlin: Springer), 57
Netzer, H., & Trakhtenbrot, B. 2007, ApJ, 654, 754
Nilson, P. 1973, Upsala General Catalogue of Galaxies (Uppsala: Astronomiska Observatorium)
Onken, C. A., Ferrarese, L., Merritt, D., Peterson, B. M., Pogge, R. W., Vestergaard, M., & Wandel, A. 2004, ApJ, 615, 645
Pence, W. 1976, ApJ, 203, 39
Peng, C. Y., Impey, C. D., Ho, L. C., Barton, E. J., & Rix, H.-W. 2006, ApJ, 640, 114
Pizzella, A., Corsini, E. M., Dalla Bontà, E., Sarzi, M., Coccato, L., & Bertola, F. 2005, ApJ, 631, 785
Postman, M., & Geller, M. J. 1984, ApJ, 281, 95
Quataert, E. 2001, in Probing the Physics of Active Galactic Nuclei, ed. B. M. Peterson, R. W. Pogge, & R. S. Polidan (San Francisco: ASP), 71
Rees, M. J. 1988, Nature, 333, 523
Richards, G. T., et al. 2002, AJ, 123, 2945
——. 2006, AJ, 131, 2766
Rossa, J., van der Marel, R. P., Böker, T., Gerssen, J., Ho, L. C., Rix, H.-W., Shields, J. C., & Walcher, C.-J. 2006, AJ, 132, 1074
Salviander, S., Shields, G. A., Gebhardt, K., & Bonning, E. W. 2007, ApJ, in press (astroph/0612568)
Sandage, A., Tammann, G. A., & Yahil, A. 1979, ApJ, 232, 352
Schechter, P. L. 1976, ApJ, 203, 297
Schmidt, M. 1968, ApJ, 151, 393
Schmidt, M. et al. 1998, A&A, 329, 495
Shakura, N. I., & Sunyaev, R. A. 1976, MNRAS, 175, 613
Shankar, F., Salucci, P., Granato, G. L., De Zotti, G., & Danese, L. 2004, MNRAS, 354, 1020
Shen, Y., Mulchaey, J. S., Raychaudhury, S., Rasmussen, J., & Ponman, T. J. 2007, ApJ, 654, L115
Simien, F., & de Vaucouleurs, G. 1986, ApJ, 302, 564
Spergel, D. N., et al. 2003, ApJS, 148, 175
Steffen, A. T., Barger, A. J., Cowie, L. L., Mushotzky, R. F., & Yang, Y. 2003, ApJ, 596, L23
Steffen, A. T., Strateva, I., Brandt, W. N., Alexander, D. M., Koekemoer, A. M., Lehmer, B. D., Schneider, D. P., & Vignali, C. 2006, AJ, 131, 2826
Stoughton, C., et al. 2002, AJ, 123, 485
Strateva, I. V., Brandt, W. N., Schneider, D. P., Vanden Berk, D. G., & Vignali, C. 2005, AJ, 130, 387
Strauss, M. A., et al. 2002, AJ, 124, 1810
Tasca, L. A. M., & White, S. D. M. 2007, MNRAS, submitted(astro-ph/0507249)
Thomas, D., Maraston, C., Bender, R., & Mendes de Oliveira, C. 2005, ApJ, 621, 673
Tinsley, B. M. 1980, ApJ, 241, 41
Trager, S. C., Faber, S. M., Worthey, G., & González, J. J. 2000, AJ, 120, 165
Tremaine, S., et al. 2002, ApJ, 574, 740
Tremonti, C. A., et al. 2004, ApJ, 613, 898
Treu, T., Malkan, M. A., & Blandford, R. D. 2004, ApJ, 615, L97
Tully, R. B., & Fisher, J. R. 1977, A&A, 54, 661
Tundo, E., Bernardi, M., Hyde, J. B., Sheth, R. K., & Pizzella, A. 2007, ApJ, in press (astroph/0609297)
Ueda, Y., Akiyama, M., Ohta, K., & Miyaji, T. 2003, ApJ, 598, 886
Ulvestad, J. S., & Ho, L. C. 2001, ApJ, 558, 561
Valluri, M., Ferrarese, L., Merritt, D., & Joseph, C. L. 2005, ApJ, 628, 137
Vanden Berk, D. E., et al. 2001, AJ, 122, 549
Veilleux, S., & Osterbrock, D. E. 1987, ApJS, 63, 295
Vestergaard, M. 2002, ApJ, 571, 733
——. 2004, ApJ, 601, 676
Voges, W., et al. 1999, A&A, 349, 389
Volonteri, M., Haardt, F., & Madau, P. 2003, ApJ, 582, 559
Wehner, E. H., & Harris, W. E. 2006, ApJ, 644, L17
Woo, J.-H., Treu, T., Malkan, M. A., & Blandford, R. D. 2006, ApJ, 645, 900
Yip, C. W., et al. 2004, AJ, 128, 585
York, D. G., et al., 2000, AJ, 120, 1579
Yu, Q., & Tremaine, S. 2002, MNRAS, 335, 965
Zakamska, N. L., et al. 2003, AJ, 126, 2125